Structure and Properties of Na₂S-SiS₂-P₂S₅-NaPO₃ Glassy Solid Electrolytes

Madison Olson^a, Steven Kmiec^b, Noah Riley^a, Nicholas Oldham^a, Kyler Krupp^b, Arumugam

Manthiram^b and Steve W. Martin^a*

^aDepartment of Materials Science and Engineering, Iowa State University of Science and Technology, 2240 Hoover Hall, 528 Bissell Rd, Ames, IA 50011, United States

^bMaterials Science and Engineering Program and Texas Materials Institute, The University of Texas at Austin, Austin, TX 78712, United States

*Email: swmartin@iastate.edu

Abstract

In the development of sodium all-solid-state batteries (ASSBs), research efforts have focused on synthesizing highly conducting and electrochemically stable solid-state electrolytes (SSE). Glassy solid electrolytes (GSEs) have been considered very promising due to their tunable chemistry and resistance to dendrite growth. For these reasons, we focus here on the atomic-level structures and properties of GSEs in the compositional series (0.6-0.08*y*)Na₂S + (0.4+0.08*y*)[(1-*y*)][(1-*x*)SiS₂+*x*PS_{5/2}]+*y*NaPO₃] (NaPSiSO). The mechanical moduli, glass transition temperatures, and temperature-dependent conductivity were determined and related to their short-range order (SRO) structures that were determined using Raman, Fourier transform infrared (FT-IR) and ³¹P and ²⁹Si magic angle spinning (MAS) nuclear magnetic resonance (NMR) spectroscopies. In addition, the conductivity activation energies were modeled using the Christensen-Martin-Anderson-Stuart (CMAS) model. These GSEs appear to be very crystallization resistant in the supercooled liquid region where no measurable crystallization below 450 °C could be observed in DSC studies. Additionally, these GSEs were found to be highly conducting, with conductivities on the order of 10⁻⁵ (Ω cm)⁻¹ at room temperature, and processable in the supercooled state without

crystallization. For all these reasons, these NaPSiSO GSEs are considered to be highly competitive and easily processable candidate GSEs for enabling sodium ASSBs.

Introduction

With increasing dependence on electric power, developing better batteries is becoming more crucial. Common batteries, such as lithium-ion batteries, for example, often employ toxic and flammable organic liquid electrolytes (OLEs), stimulating the development of solid-state electrolytes (SSEs) as safer alternatives. ¹⁻² In addition to OLEs, batteries are often designed using expensive, rare, and even unethically sourced materials like lithium metal and cobalt. ³⁻⁴ Sodium all-solid-state (ASSBs) batteries have been pursued as a solution to these ethical and environmental concerns. These issues have led to exploring batteries using only low cost, abundant materials like sodium and sulfur. ⁵⁻⁶ The SSE separator has, in particular, been the subject of considerable research focus and interest.

One class of sodium SSEs is based on oxide ceramics, such as sodium beta-alumina and NASICON (Na₃Zr₂Si₂PO₁₂). These materials have high ionic conductivities and good chemical and electrochemical stability, making them promising candidates for use in sodium ASSBs.⁷⁻⁸ Another class of sodium SSEs is based on polymers, such as polyethylene oxide (PEO) and its derivatives. These materials can offer improved mechanical flexibility compared to ceramic electrolytes, but often have lower ionic conductivities.⁹ While there are many classes of SSEs, amorphous materials show unique merit.

Sulfide glassy solid electrolytes (GSEs) can offer high ionic conductivities and inherent resistance to dendrites but may be more difficult to process and manufacture compared to ceramic and polymer electrolytes due to their poor air stabilty. ¹⁰⁻¹³ The composition of the SSE plays a crucial role in determining its properties. The tunable compositions of GSEs allow for the fine

control of its ionic conductivity, chemical stability, and mechanical toughness. Mixed glass former (MGF) systems have been shown to improve the glass formability and sometimes the ionic conductivity, while mixed anion systems have been shown to improve the thermal and chemical stabilities. ^{11, 14-16} For example, the MGF system Li_{1.5+x}Al_{0.5}Ge_{1.5}Si_xP_{3-x}O₁₂ and mixed anion system Na₃PS_{4-x}O_x based amorphous SSE systems have both found benefits to conductivity and chemical stability with increased x, respectively. ^{10, 17} Further, silicate-rich systems have not only shown improved ionic conductivity, but also lower parasitic electronic conductivity and higher electrochemical stability. ¹⁸⁻²⁰ For example, the Na₂S-SiS₂-PS_{5/2} system studied by Watson *et al.* showed highly competitive conductivities on the order of 10⁻⁵ at room temperature. ²⁰ In addition to the Na₃PS_{4-x}O_x system, many other mixed anion GSE systems have shown benefits of incorporating oxygen into a pure sulfide glass. ¹⁰ For example, the Li₂S-SiS₂-Li₃PO₄ and the Na₂S-P₂S₅-P₂O₅ GSEs studied by Tatsumisago *et al.* and Kmiec *et al.*, respectively, both showed improved ionic conductivity with oxygen doping. ²¹⁻²²

The system studied here, $zNa_2S+(1-z)[(1-y)[(1-x)SiS_2+xPS_{5/2}]+yNaPO_3]$, (NaPSiSO) was selected to combine the beneficial properties of MGF and mixed anion GSE systems. The GSEs in this NaPSiSO series were studied to identify the relationships between their short-range order (SRO) structures and their physical properties. A detailed investigation of their atomic-level structures was completed using Raman, Fourier Transform Infrared (FT-IR), and ³¹P and ²⁹Si magic angle spinning (MAS) nuclear magnetic resonance (NMR) spectroscopies. Their thermal behavior and sodium ion transport properties, important determinations for applications as GSEs, were found utilizing differential scanning calorimetry (DSC) and electrochemical impedance spectroscopy (EIS), respectively. Lastly, the conductivity-activation energies were modeled using the Christensen-Martin-Anderson-Stuart (CMAS) model.

The SRO structures revealed that the phosphorus species are found in all non-networking structures (P^0), whereas silicon was found to disproportionally form non-networking (Si^0) and networking (Si^2) chemical species. Here, the superscript refers to the number of network-forming (bridging) bonds of oxygen or sulfur. Additionally, at low oxygen concentrations, almost all of the oxygen was coordinated around silicon. At higher oxygen concentrations, however, the oxygen ordered approximately randomly between the two glass formers, silicon and phosphorus. These GSEs were found to be highly resistant to crystallization, where, interestingly, no GSE in the NaPSiSO series showed a crystallization exotherm. The NaPSiSO GSEs were also found to be highly conducting, where glasses with a high concentration of silicon and low concentration of oxygen had room temperature sodium-ion conductivities higher than 10^{-5} (Ω cm)⁻¹. These results were consistent with the modeled conductivity activation energies determined using the Christensen-Martin-Anderson-Stuart (CMAS) model. As a result of these promising properties, these compositions in the NaPSiSO series present several advantages toward application as GSEs for sodium ASSBs.

Experimental Methods

Materials Synthesis

Glasses in the series, $z\text{Na}_2\text{S}+(1-z)[(1-y)[(1-x)\text{SiS}_2+x\text{PS}_{5/2}]+y\text{NaPO}_3]$, were synthesized within the bounds of $0.57 \le z \le 0.588$, $0 \le y \le 0.35$, and $0.15 \le x \le 0.35$. The bounds on z were determined to simplify the glass series such that all compositions (x, y) would maintain a constant R-value (moles of Na / moles of Si and P) equal to 3, independent of y. Due to the dependence of z on y to maintain z for all glasses, the glass series was re-written, as shown above, to z on z

in these compositionally complicated GSEs, **Table S1** summarizes the molar compositions of each glass made as well as their x and y values and corresponding O/(O+S) and P/(P+Si) ratios.

Batches of 5 g of glasses were prepared in a N₂ atmosphere glovebox (< 5 ppm O₂ and H₂O). One sample of each composition was made, with some samples made in triplicate for error analysis of the GSEs. The raw materials consisted of phosphorus pentasulfide (P₂S₅ 98% Acros Organics), sodium sulfide (Na₂S 99.9% Alfa Aesar), silicon sulfide (synthesized in-house), and sodium metaphosphate (NaPO₃ synthesized in-house). NaPO₃ was used as the source of oxygen due to its simple and cost-effective synthesis process.

The NaPO₃ was synthesized using the standard melt-quenching technique from stoichiometric amounts of the starting materials, sodium carbonate (Na₂CO₃, 99.5% Sigma Aldrich) and ammonium phosphate dibasic ((NH₄)₂HPO₄, 99+% Acros Organics). Silicon sulfide (SiS₂) was synthesized through a combination of silicon (Si, Alfa Aesar 99.9985% metals basis) and excess sulfur (S, Alfa Aesar 99.999% metals basis). These starting materials were thoroughly mixed in a stainless-steel mill pot with a single ball using a Spex 8000 M Mixer/Mill before being placed into a silica quartz ampoule. The ampoule was then sealed under vacuum and placed into a furnace, which was rotated at an angle of 15°. The ampoule was heated from 25 to 970 °C at a rate of 1 °C min⁻¹ over a period of 52 hours before slowly cooling back to room temperature. After this heating profile, the S + SiS₂ mass was heated in a vertical tube furnace for 8 hours at 675 °C with the S + SiS₂ mass situated in the hot zone of the furnace and the opposite end of the ampoule placed outside of the furnace. This created a temperature profile in the ampoule that caused the excess sulfur to be distilled off the SiS₂ reaction product. The SiS₂ was then removed from the ampoule inside of a N₂ glove box and stored for later use.

Both the Na₂S and the SiS₂ were considered to be of nominally high purity, however, each material was heat treated on the same day of use to expunge any possible excess sulfur at 750 °C and 900 °C, respectively, for 15 minutes in vitreous carbon crucibles inside a horizontal tube furnace hermetically sealed to the side of the glove box. Stoichiometric amounts of all starting materials were then milled inside a stainless steel mill pot with a single stainless steel ball using a Spex 8000M Mixer/Mill at 1725 rpm for 5 minutes. The glass batch was then melted twice for 15 minutes each at temperatures ranging from 775 to 800 °C depending on composition inside a covered vitreous carbon crucible inside the same tube furnace described above. The first melt was used to determine if there was any disadvantageous weight loss of the glass batch on melting after cooling to room temperature, typically < 2 wt.%, and a second melt was used to ensure a homogenous liquid was achieved before quenching between two brass plates. All samples were quenched to red, visually homogonous pieces, approximately 1 mm or less in thickness. Note that error bars in the data represent the standard error of these samples made. Not all samples have error bars as not every sample was made in triplicate. These melt-quenched (MQ) glass samples were stored and handled in an inert atmosphere of a glove box filled with N₂, with levels < 5 ppm O₂ and H₂O.

Differential Scanning Calorimetry

Bulk pieces of MQ glass, approximately 2 - 12 mg, were sealed in hermetic aluminum pans for DSC measurements. Measurements were made between 50 and 450 °C at 20 °C min⁻¹ to determine the glass transition temperature, T_g , of each sample. To extract the T_g of the sample using a known thermal history, each sample was packed using a different specimen of glass and ran a second time. This sample was then cycled 50 °C past the T_g three times, and heated a fourth time up to 450 °C, the upper limit of the DSC, to not only determine the T_g reported but also the

crystallization and melting temperatures, T_c and T_m , respectively, if present. In no compositions of this NaPSiSO series, however, were crystallization exotherms observed.

Powder X-Ray Diffraction

Powder X-ray diffraction (PXRD) was run on a select number of the GSEs to determine the extent of crystallization, if any, that occurred during synthesis. Samples of MQ glass were ground to fine powders and packed onto a zero-background silicon wafer, which was sealed in a Bruker air-tight sample holder. The PXRD measurement was made with a Rigaku SmartLab X-ray Diffractometer from 2θ values of 20° to 90° with a step width of 0.1° and scan speed of 5° min⁻¹ for an 18-minute scan duration. All samples tested showed no evidence of crystallization, **Figure S1**.

Density and Longitudinal and Transverse Sound Velocity Measurements

The mechanical moduli of each glass in the NaPSiSO series were determined from density and sound velocity measurements. The densities of all of the glasses were measured using the Archimedes method. Due to the air and water sensitivity of these GSEs, all density measurements were performed inside an argon glove box with mineral oil of known density as the suspension liquid. The samples used were the same discs used for conductivity measurements, see below. The mechanical moduli were measured by first measuring the thickness of a polished sample across different points of the disc shaped glass sample. Next, the longitudinal (V_L) and transverse sound velocities (V_T) were measured using an Ultratek EUT3160 Pulser/Receiver configured as a thickness probe equipped with 15 and 5 MHz contact transducers with Vaseline and phenyl salicylate (Salol) as coupling agents for longitudinal and transverse waves, respectively. The mechanical moduli and the Poisson's ratio of each GSE was then calculated from these four measured parameters, thickness (t), density (ρ), V_L and V_T , using **Equations 1 - 5**, shown below.

Electrochemical Impedance Spectroscopy

The temperature dependent sodium ion conductivity was measured on glass samples cast and annealed into \sim 15 mm disks with a maximum thickness of \sim 2.5 mm. These samples were dry polished to a \sim 1 μ m grit surface finish and sputtered with gold blocking electrodes (Au | GSE | Au) 10 mm in diameter using an Anatech Hummer VI sputtering system. Each cast, polished, and sputtered disk was sealed in a custom hermetic sample holder for variable temperature conductivity measurements using a Novocontrol Concept 80 dielectric spectrometer equipped with a cryostat. Each sample was measured in a frequency range of 0.1 Hz to 10 MHz from temperatures of -60 to 150 °C. The d.c. sodium ion conductivity was determined by best fitting the complex impedance using an equivalent circuit of a parallel circuit of a constant phase element and a resistor in series with a Warburg element for pile-up of ions on the blocking, gold electrodes.

Raman Spectroscopy

Pieces of MQ glass were sealed in a hermetic tray under a N₂ atmosphere to determine the Raman spectrum of each glass. The tray's lid was a standard soda lime silicate glass microscope slide. Measurements were made using an inVia 488 nm Renishaw Coherent Laser Raman Microspectrometer. The instrument was calibrated using the main intense peak centered at 520.5 cm⁻¹ (±0.4) of an internal silicon reference before the sample measurements. Each spectrum was collected between 200 cm⁻¹ and 1,500 cm⁻¹ using a 20x objective lens, 10 s exposure, and 12.5 mW power. Each sample was measured twice in different locations to ensure the sample was homogeneous, and each measurement had a maximum of 15 accumulations.

Fourier Transform Infrared Spectroscopy

Samples of MQ GSEs were prepared for FT-IR by diluting the GSE in cesium iodide (CsI) in a mass ratio of ~ 1 : 40. The GSE sample and CsI mixtures were ground to fine powders with a

mortar and pestle and pressed into a thin pellet, $\sim 100~\mu m$ thick, to enable these samples to be measured in transmission mode. The samples were transferred to the FT-IR in a sealed container and kept under N_2 flow before being placed into the vacuum chamber of the spectrometer. A Bruker Vertex 80v FT-IR spectrometer was used to collect the FT-IR spectra under vacuum from $400~cm^{-1}$ to $4{,}000~cm^{-1}$ using a potassium bromide beam splitter. Measurements were obtained with $4~cm^{-1}$ resolution and 32 accumulations.

Nuclear Magnetic Resonance Spectroscopy

All GSE samples were ground into powder with a mortar and pestle in an argon-filled glovebox prior to packing 4 mm zirconia rotors for solid-state MAS NMR experiments. The ²⁹Si and ³¹P MAS NMR experiments were performed on a 400 MHz ($B_0 = 9.4$ T) Bruker Avance III HD spectrometer equipped with a broadband double resonance HX 4 mm probe. All experiments were conducted with a MAS rotation speed of 12.5 kHz. The ²⁹Si MAS NMR spectra were collected by co-adding 800-1500 transient scans, depending on the sample, each with a recycle delay of 75-90 s, a pulse length of 3.5 μ s, and pulse power of 200 W. The ³¹P MAS NMR spectra were collected by co-adding 96 transient scans, each with a recycle delay of 360 s, a pulse length of 3.5 μ s, and pulse power of 200 W. All spectra were indirectly referenced to tetramethylsilane (TMSS) ($\delta iso = 0$ ppm) using the unified scale in the IUPAC standard.²³

Results

Differential Scanning Calorimetry

Each glass in the NaPSiSO series had a measurable T_g , **Figure 1**. In this entire series, no crystallization and, therefore, no subsequent melting transitions could be observed up to 450 °C, which was the upper limit of the DSC used to make these measurements, see **Figure 1A**. Assuming that the "2/3 rule" for T_g and T_l , where T_l is the liquidus temperature, holds for these compositions,

a nominal T_g of 275 °C would put T_l at ~ 550 °C and this suggests that these compositions are highly resistant to crystallization below their T_l . ²⁴ Figure 1B shows that the measured T_g for each GSE decreases with both x (PS_{5/2}) and y (NaPO₃). For a common x-value, the T_g 's were the highest for the glasses with the highest concentration of silicon and lowest amount of NaPO₃ (y = 0.15), but as y increased, the T_g decreased, Figure 1B. PXRD was run to ensure full glassy character of the GSEs in the NaPSiSO series. The PXRD patterns of a select number of samples showed no crystalline peaks as can be found in Figure S1.

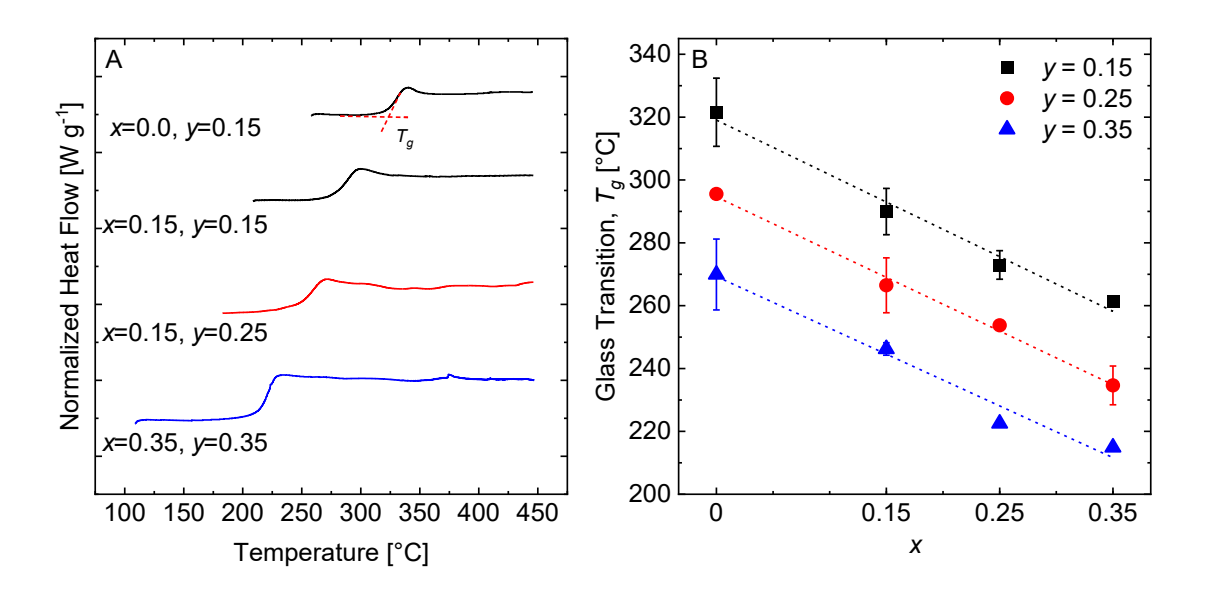


Figure 1: A) DSC thermograms of a few glasses in the (0.6-0.08y)Na₂S + (0.4+0.08y)[(1-y)[(1-x)SiS₂+xPS_{5/2}]+yNaPO₃] (NaPSiSO) series. **B)** T_g s of all of the GSEs in the NaPSiSO series. Error bars represent the standard error among all measurements of at least three different samples.

Density and Ultrasonic Testing

The density and mechanical moduli of the GSEs in the NaPSiSO series were determined and are shown in **Figures 2A-D**. The density, ρ (g cm⁻³), was determined using the Archimedes method. The longitudinal, L (GPa), and shear moduli, G (GPa), were determined from their relationship to the longitudinal, V_L (mm μ s⁻¹), and transverse, V_T (mm μ s⁻¹), sound velocities,

Equations 1-2, respectively. Poisson's ratio, v, and the Young's modulus, E, were calculated using Equations 3-4, respectively. The bulk modulus, K, was calculated from the two moduli, E and E0, Equation 5. The values for the E0, sample thickness, E1 and E2 and E3 well as E4 and E5.

$$(1) L = \rho(V_L)^2$$

$$(2) G = \rho(V_T)^2$$

$$(3) v = \frac{L - 2G}{2(L - G)}$$

$$(4) E = (1+\nu)2G$$

$$(5) K = L - \frac{4}{3}G$$

In **Figures 2A-D**, the ranges of the y-axis scales are relatively small for all of the values due to the relatively small changes in composition made across the NaPSiSO series, but the general trends in the density and moduli are consistent, **Figure 2**, and larger than the standard error of the measurements. The density and all moduli increase with increasing y, where the value of y represents added NaPO₃ to the NaPSiSO series. The Poisson's ratio are consistent with literature on highly modified GSEs and decrease with increasing y, which fits the decrease in network strength with added phosphorus, see below.²⁵ The trends are less observable with the changes in x (added PS_{5/2}).

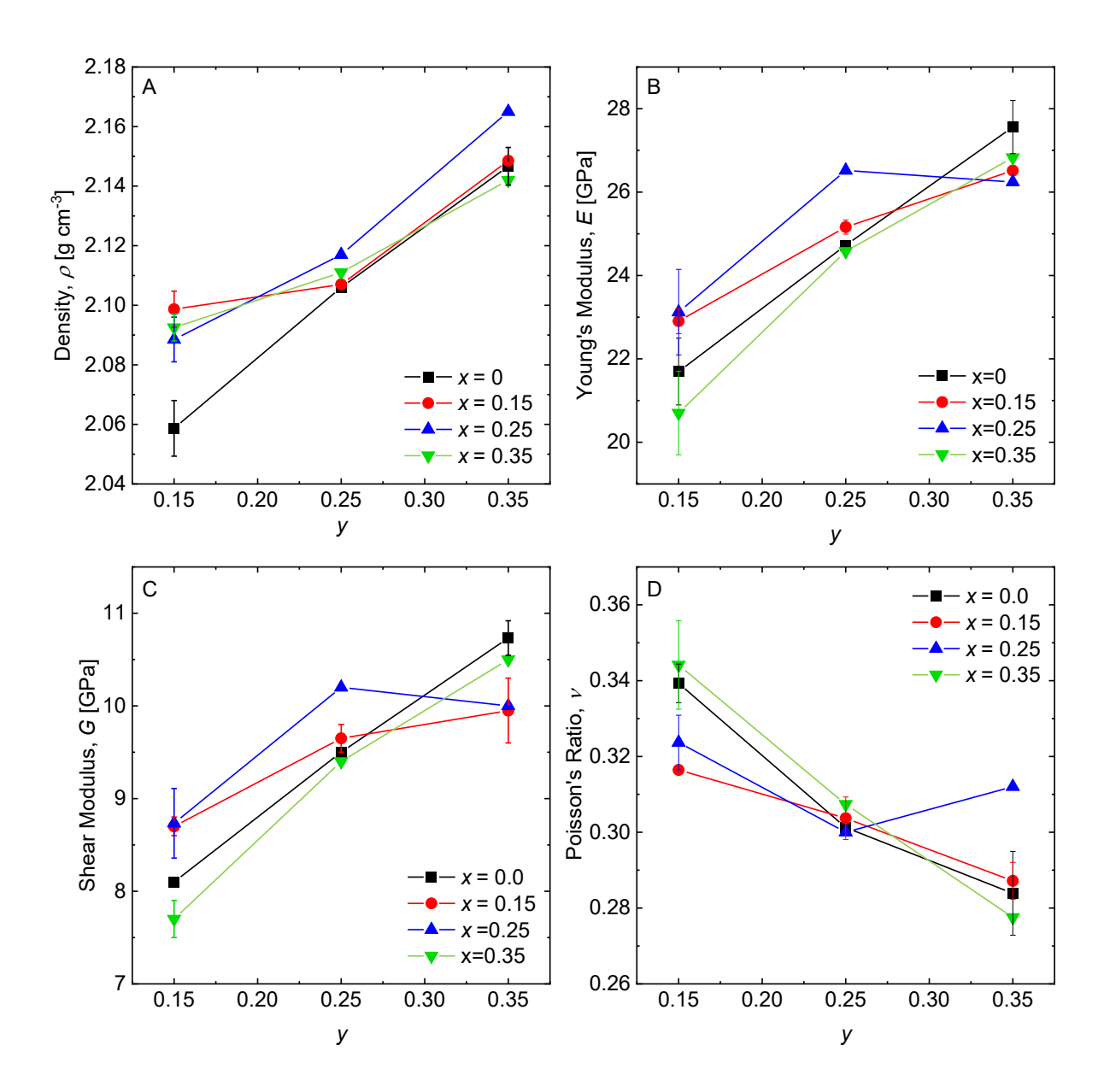


Figure 2: The **A)** density, **B)** Young's modulus, **C)** shear modulus, and **D)** Poisson's ratio of the glasses in the $(0.6\text{-}0.08y)\text{Na}_2\text{S} + (0.4\text{+}0.08y)[(1\text{-}y)[(1\text{-}x)\text{SiS}_2\text{+}x\text{PS}_{5/2}]\text{+}y\text{NaPO}_3]}$ (NaPSiSO) series. Error bars represent the standard error between measurements of different samples.

Electrochemical Impedance Spectroscopy

Figures 3A-B show the Nyquist plots for the x = 0.15, y = 0.15 GSE for a selection of different temperatures and the equivalent circuit used to model and fit the data, respectively. Best-fitting of the complex impedance experimental data to the equivalent circuit yielded the bulk

resistance, R_{bulk} , at each temperature. The temperature dependent d.c. sodium ion conductivity, $\sigma_{d.c.}$, was then determined from the known relationship given in, **Equation 6**

$$\sigma_{d.c.} = \frac{1}{R_{bulk}} \left(\frac{t}{A} \right)$$

where, *t* is the thickness of the GSE sample, and *A* is the area of the sputtered gold electrode. The Nyquist plots, **Figure 3A**, for temperatures of 25, 30, 45, and 60 °C show the typical semi-circle arcs in the complex impedance arising from the combined conduction and polarization mechanisms of the GSE followed by polarization due to the blocking gold electrodes.

To elucidate the trends in the temperature-dependent sodium ion conductivity, the simplified Arrhenius plots for glasses with constant x and y are shown in **Figures 3C-D**, respectively. The same plots for the remaining GSEs in the NaPSiSO series can be seen in **Figure S2**.

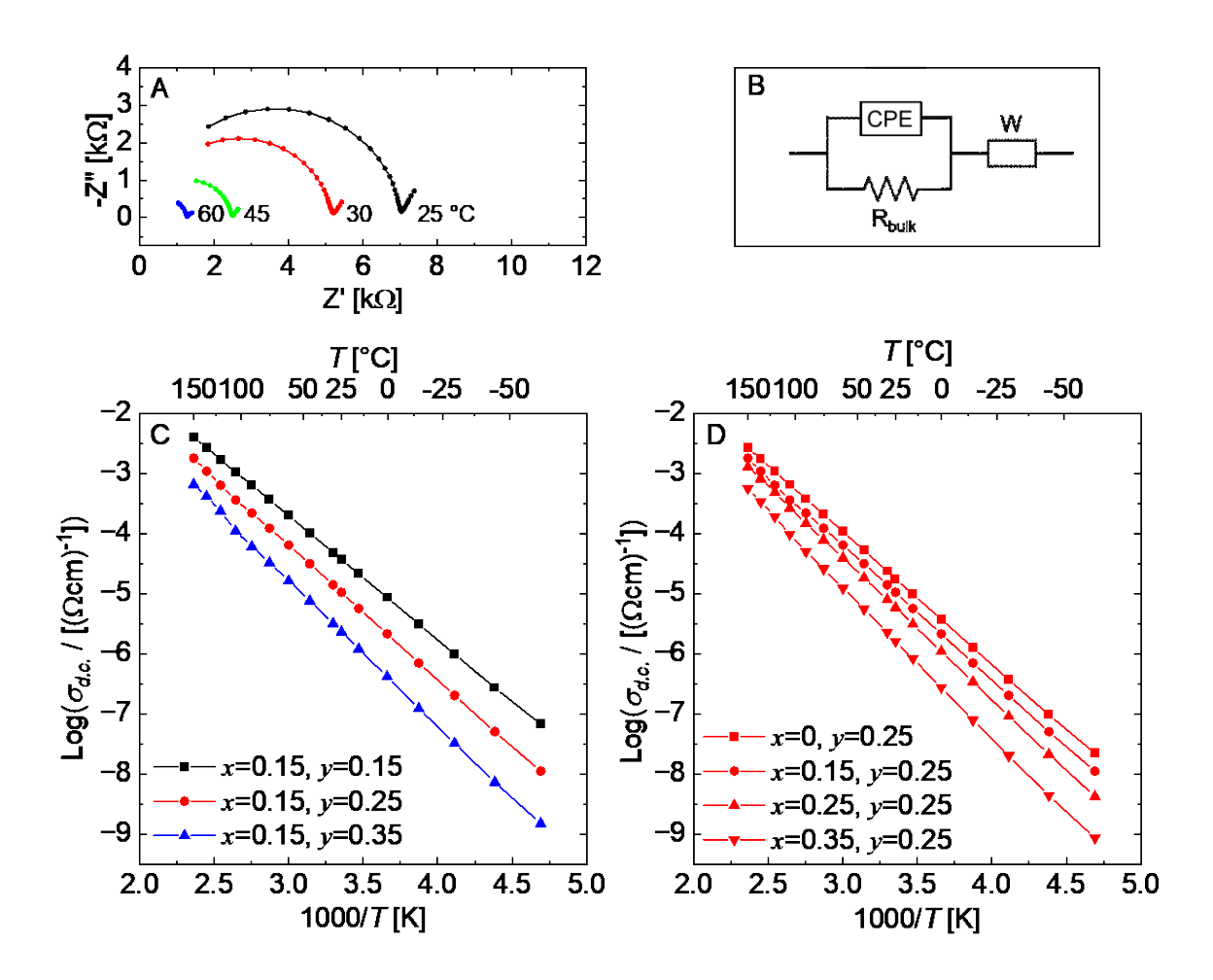


Figure 3: A) Nyquist plot for the x = y = 0.15 NaPSiSO GSE at variable temperatures. **B)** R-CPE-W equivalent circuit used to fit the Nyquist plots. **C)** Arrhenius plots of the d.c. sodium ion conductivity, $\sigma_{d.c.}$, for x = 0.15, y = 0.15, 0.25, 0.35 glasses. **D)** and y = 0.25, x = 0.0, 0.15, 0.25, 0.35 glasses in the (0.6-0.08y)Na₂S + (0.4+0.08y)[(1-y)[(1-x)SiS₂+xPS_{5/2}]+yNaPO₃] (NaPSiSO) series. The simplified log($\sigma_{d.c.}$) vs. 1000/T Arrhenius plots are shown here to easily read the conductivities directly from the graph. The full Arrhenius plots were used to determine the conductivity activation energies, see below.

Figure 3C shows that as NaPO₃ is added to the series, increasing y at constant x, increasing the amount of added oxygen and phosphorus in the system, the conductivity decreases. **Figure 3D** shows that as SiS₂ is substituted for PS_{5/2}, increasing x at constant y, the conductivity decreases. The sodium ion conductivity, $\sigma_{d.c.}$, at 75 °C and the conductivity activation energy, ΔE_{act} , were

determined for all glasses in the NaPSiSO series, **Figure 4**, by fitting the conductivity to the full Arrhenius equation, **Equation 7**

(7)
$$\sigma_{d.c.}T = \sigma_0 \exp\left(-\frac{\Delta E_{act}}{RT}\right)$$

where $\sigma_{d.c.}$ is the ionic conductivity, σ_{0} is the pre-exponential factor, R is the gas constant and T is the temperature.²⁶ The composition dependence of the $\sigma_{d.c.}$ for all of the NaPSiSO GSES at 105, 25, and -30 °C can be found in **Figure S4**.

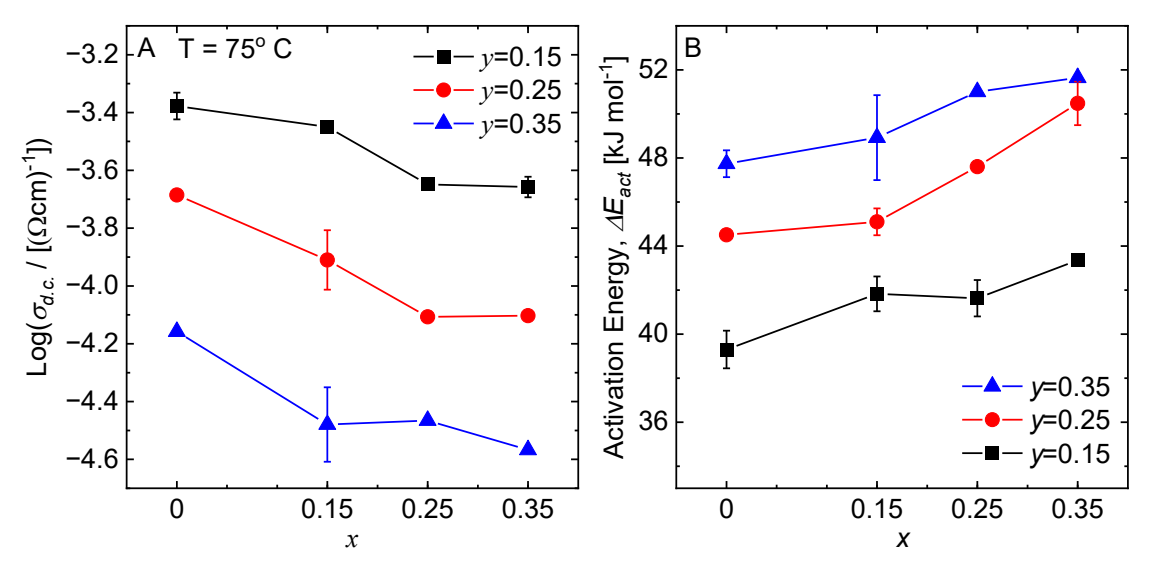


Figure 4: A) Sodium ion conductivity, $\sigma_{d.c.}$ at 75 °C and **B)** conductivity activation energy, ΔE_{act} , for GSEs in the $(0.6\text{-}0.08y)\text{Na}_2\text{S} + (0.4\text{+}0.08y)[(1\text{-}y)[(1\text{-}x)\text{SiS}_2+x\text{PS}_{5/2}]+y\text{NaPO}_3]}$ (NaPSiSO) series. Error bars represent the standard error between original measurements of different samples. The activation energies were obtained from the slope of a $\ln(\sigma T)$ vs. 1000/T plots, see **Figure S3**.

The $\sigma_{d.c.}$ at 75 °C shows the same trends; the conductivity is highest for the compositions with the most SiS₂ and the least added phosphorus and oxygen where, as NaPO₃ is added to the GSE series, the conductivity decreases (increasing y). The ΔE_{act} follows an expected trend in the $\sigma_{d.c.}$, where glasses with higher $\sigma_{d.c.}$ have lower ΔE_{act} .

In addition to the ionic conductivity, the relative permittivity, ε_{∞} , was also determined for all the glasses in the NaPSiSO series. This was done by determining the real part of the

permittivity, ε' , as a function of temperature and frequency, and ε_{∞} was determined at the lowest temperature, -55 °C, and highest frequency measured, 1 MHz, see **Figure 5A**, where $\varepsilon' \to \varepsilon_{\infty}$. The ε_{∞} follows the expected trend, where added oxygen with is lower atomic polarizability decreases the relative permittivity value, **Figure 5B**.^{22,27}

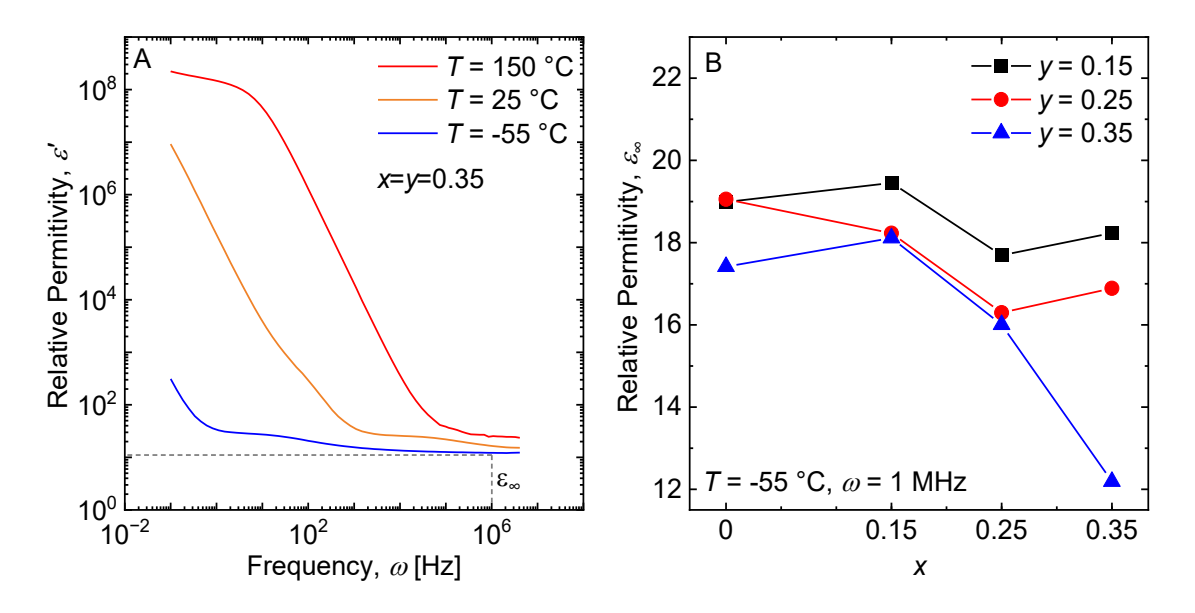


Figure 5: A) Frequency and temperature dependence of the relative permittivity, ε' , for the x = 0.35, y = 0.35 glass at 150, 25, and -55 °C in the GSE (0.6-0.08y)Na₂S + $(0.4+0.08y)[(1-y)[(1-x)SiS_2+xPS_{5/2}]+yNaPO_3]$ (NaPSiSO) series. The permittivity at -55 °C and 1 MHz was taken as the ε_{∞} for the GSE. **B)** The ε_{∞} for all GSEs in the NaPSiSO series.

Raman and FT-IR Spectroscopy

The Raman and FT-IR spectra were collected for all glasses in the NaPSiSO series, **Figure** 6. The Raman spectra, **Figures 6A-C**, show modes associated with sulfide and MOS chemical species in the GSE series. Structural depictions of the SRO units can be found in **Table S3**. From here on, the superscripts define the number of bridging anions on the SRO structure. The most intense peak in the Raman spectra for all the GSEs studied is centered at 421 cm⁻¹ and is assigned to the symmetric stretching of P⁰ (phosphorus species with no shared corners) sulfide chemical species, PS₄³⁻ and MOS PS₃O³⁻ species, see **Figure S5**.²⁸⁻³¹ The peak spanning the range of 380 -

410 cm⁻¹ is associated with the symmetric stretch of Si⁰, SiS₄⁴, and edge-sharing E¹Si², Si₂Si₆⁴, sulfide species, at 395 cm⁻¹ and 405 cm⁻¹, respectively.^{19, 32-33} Here, the E¹ notation indicates that this Si² species shares one edge with 2 bridging sulfurs (BSs). Present in only some of the GSEs, the very weak shoulder at 436 cm⁻¹ is assigned to the symmetric stretching mode of the polysulfide Na₂S₅.³⁴⁻³⁵ The peak centered at 470 cm⁻¹ arises from an impurity found in all of these NaPSiSO GSEs in varying amounts is assigned to the symmetric stretching of the homopolar -S-S- bonds.³⁵⁻³⁶ Two shoulders straddling this mode at 461 and 478 cm⁻¹ arise from the symmetric stretch of Na₂S₂ and Na₂S₄ ionic polysulfide species, respectively.³⁵⁻³⁶ The amount of this sulfur/polysulfide impurity was estimated to be 2.5 wt.%. The methodology to determine this value is shown in **Figure S6.** Its significance, primarily on the electrochemical properties of these GSEs, will be examined and reported in future publications. The last peak of note in the Raman spectra is centered at 556 cm⁻¹ and is assigned to the symmetric stretch of the MOS species PS₂O₂^{3-,31}

The FT-IR spectra, **Figures 6D-F**, show sulfide, oxide, and MOS modes in the GSE series. The main mode in the IR spectra for all samples is the strong peak at 560 cm⁻¹ and is attributed to the bending mode for the BS species, $\delta(\text{Si-S-Si})$, and the asymmetric stretch of P⁰ PS₄³⁻ and PS₂O₂³⁻ species. Two shoulders are observed on this main peak at 497 cm⁻¹ and 620 cm⁻¹ and are attributed to the bending mode of non-bridging oxygen (NBO) species $\delta(\text{^-O-Si-O^-})$ and to the asymmetric stretch of E¹ Si₂S₆⁴⁻ chemical species, respectively. The absorbance at 670 cm⁻¹ is assigned to the non-bridging sulfur (NBS) in Si⁰ species, Si-S⁻ bonds and the absorbance band at ~700 cm⁻¹ is assigned to the NBS, P=S, of P⁰ chemical species PSO₃³⁻. 31, 38

At higher wavenumbers, there are peaks between 800 and 1,200 cm⁻¹ and while the spectra for some of the GSEs show less distinction and resolution in this region, the overall peak analysis remains the same across all of the GSEs in this series. All of these peaks arise from oxygen bonded

to Si and P. The peak at 924 cm⁻¹ is assigned to the asymmetric stretch of NBO species, $v_{as}(\equiv Si-O^-)$. ⁴¹ The peaks at and 950 cm⁻¹ and 990 cm⁻¹ are assigned to the NBOs of Si⁰, Si-O⁻ bonds, and O=P-O⁻, respectively. ⁴²⁻⁴³ The highest wavenumber peaks in the IR spectra at 1,040 cm⁻¹ and 1,095 cm⁻¹ are assigned to the BOs in Si² units and the symmetric stretch of BO Si-O-Si, respectively. ^{42,43}

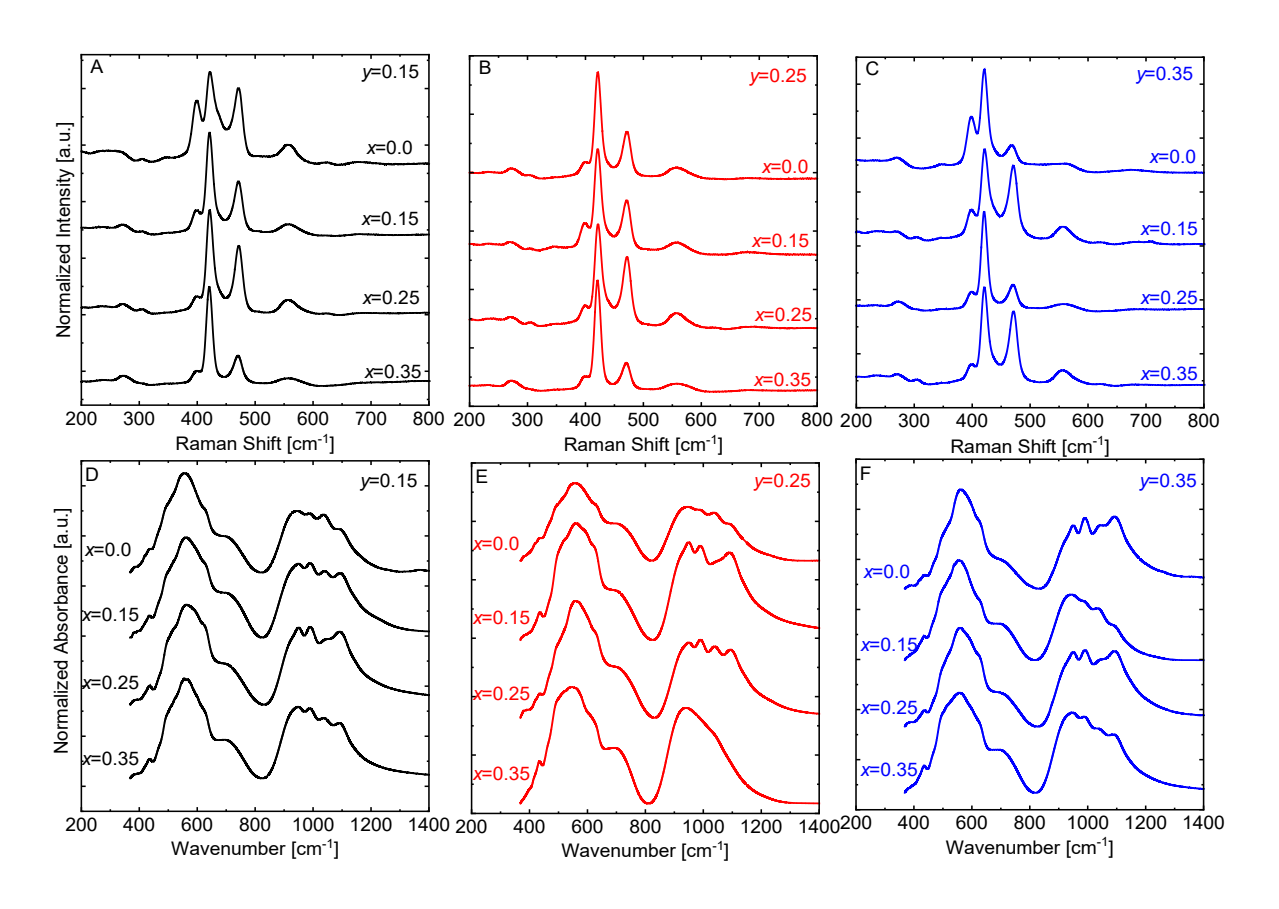


Figure 6: A-C) Raman and **D-F)** FT-IR spectra for all glasses in the (0.6-0.08y)Na₂S + $(0.4+0.08y)[(1-y)[(1-x)SiS_2+xPS_{5/2}]+yNaPO_3]$ (NaPSiSO) series.

³¹P and ²⁹Si MAS NMR

The 31 P and 29 Si MAS NMR spectra were collected for all of the GSE samples in the NaPSiSO series, **Figures 7A-F**. Again, for a reference, the structural depictions of each of the SRO chemical species are provided in **Table S3**. The 31 P MAS NMR spectra, shown in **Figures 7A-C**, show a main peak centered at 87 ppm, which is assigned to 90 PS₄³⁻ anions for the y = 0.15

glasses.^{10, 45} For glasses with higher oxygen concentrations, y = 0.25 and 0.35, this peak is also assigned in part (50%) and fully to the MOS species in the higher y GSEs, P^0 PS₃O³⁻ anions, respectively.^{10, 45-46} This unique dual assignment has been confirmed through a careful assessment of the chemical shift anisotropy (CSA) values for the glasses with higher NaPO₃ contents (y = 0.25 and 0.35) as they are shown to increase, suggesting the presence of the P^0 PS₃O³⁻ anion in these compositions, see **Figure S7**. For all of the GSEs, x and y, the two peaks at 63 and 35 ppm are assigned to MOS chemical species, P^0 PS₂O₂³⁻ and P^0 PSO₃³⁻ anions, respectively.^{10, 45} For glasses with higher oxygen concentrations, y = 0.25 and 0.35, two additional peaks arise at 17 and 3.6 ppm and are assigned to the pure oxide P^0 PO₄³⁻ and P^1 P₂O₇⁴⁻ anions, respectively.⁴⁷

The 29 Si MAS NMR spectra, **Figures 7D-F**, show additional structural information for these GSEs that arises from the second glass former, silicon. First, the predominant peak at -0.5 ppm is assigned to the Si⁰ SiS₄⁴⁻ anion. ^{45, 48} At 5 ppm, the defect species Si^{1Si} Si₂S₆⁶⁻, so-called because it has a direct Si-Si bond, see **Table S3**, is present in some of the glasses. ⁴⁹ The peak centered at \sim -13 ppm is in fact a doublet and the two peaks are assigned to the corner sharing Si² SiS₃²⁻ species and the edge sharing E¹ Si₂S₆⁴⁻ species, each centered at -11 and -15 ppm, respectively. ⁴⁸ The peaks centered at -32 and -40 ppm have been assigned to the MOS Si⁰ SiS₂O₂⁴⁻ and corner sharing Si² SiS₂O²⁻ chemical species, respectively. ^{19, 40} A second doublet with peaks centered at -67 and -76 ppm have been assigned to the Si⁰ SiSO₃⁴⁻ and corner sharing SiSO₂²⁻ chemical species. ^{19, 40, 50}

Spectral deconvolutions of one ³¹P and one ²⁹Si MAS NMR spectra of the GSEs, consistent with the ³¹P and ²⁹Si MAS NMR spectra of all of the other GSEs in the NaPSiSO series, are shown in **Figures 8A-B.** Spectral deconvolutions of other GSEs can be found in **Figure S8.** A summary

of the peak assignments, the relative populations of the various SRO species, spectra widths, and CSA values for a selection of the NaPSiSO GSEs are shown in **Tables S4-S5**.

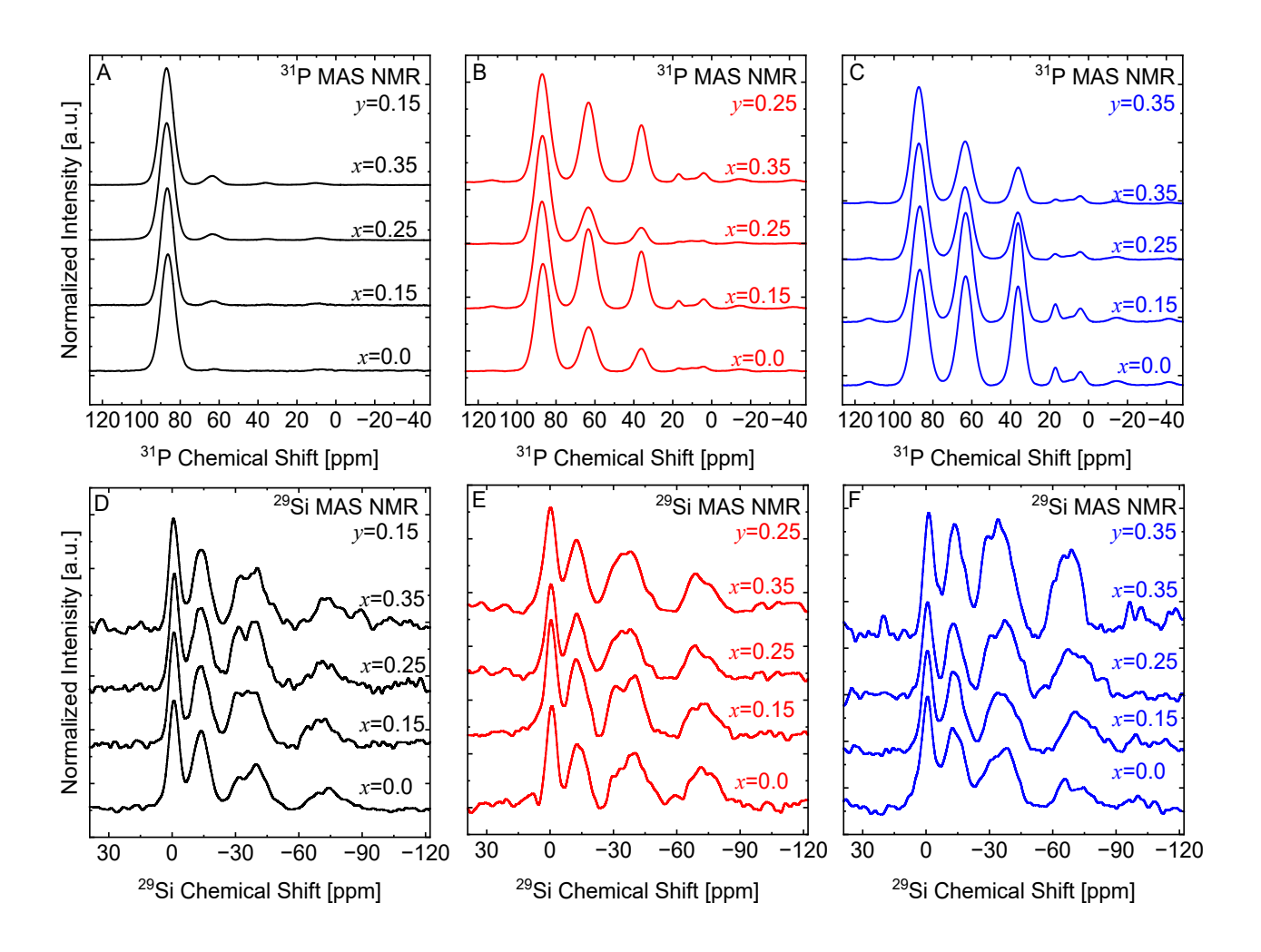


Figure 7: A-C) ³¹P MAS NMR and **D-F)** ²⁹Si MAS NMR spectra for all glasses in the (0.6-0.08*y*)Na₂S + (0.4+0.08*y*)[(1-*y*)[(1-*x*)SiS₂+*x*PS_{5/2}]+*y*NaPO₃] (NaPSiSO) series.

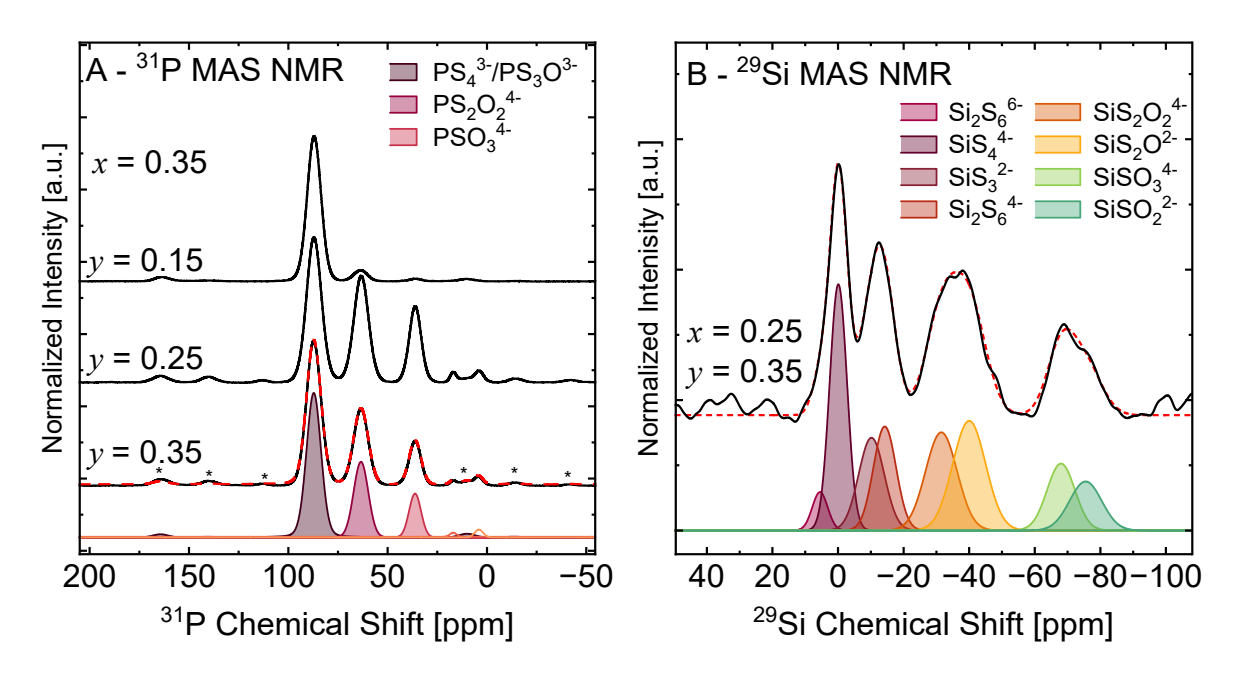


Figure 8: A) ³¹P MAS NMR deconvolution for the x = 0.35, y = 0.15, 0.25, 0.35 GSEs and **B)** ²⁹Si MAS NMR deconvolution for the x = 0.25, y = 0.35 GSE in the (0.6-0.08y)Na₂S + (0.4+0.08y)[(1-y)[(1-x)SiS₂+xPS_{5/2}]+yNaPO₃] (NaPSiSO) series.

Discussion

Structural Analysis of NaPSiSO GSEs

The 31 P and 29 Si MAS NMR spectra of each GSE has been deconvoluted in a similar way to the GSE samples shown in **Figure 8** and through this, the absolute percentage of each SRO chemical species in each NaPSiSO GSE have been determined from the 31 P and 29 Si MAS NMR spectra, **Figures 9A-F**, respectively. Interestingly, the 29 Si MAS NMR spectra show that the general trend among the silicon species is that the relative amounts of the different species present in the GSEs remain consistent for all the samples in the NaPSiSO series, they just decrease in their total amount as phosphorus is added to the composition with increasing x (added PS_{5/2}) and y (added NaPO₃), **Figures 9A-C**. Different than this, the 31 P MAS NMR spectra reveal the phosphate SRO species show a more dramatic structural shift from mostly pure sulfide SRO species in the y 0.15 GSEs, **Figure 9D**, to more MOS SRO species in the y = 0.25 and y = 0.35 NaPSiSO GSEs, **Figures 9E-F**.

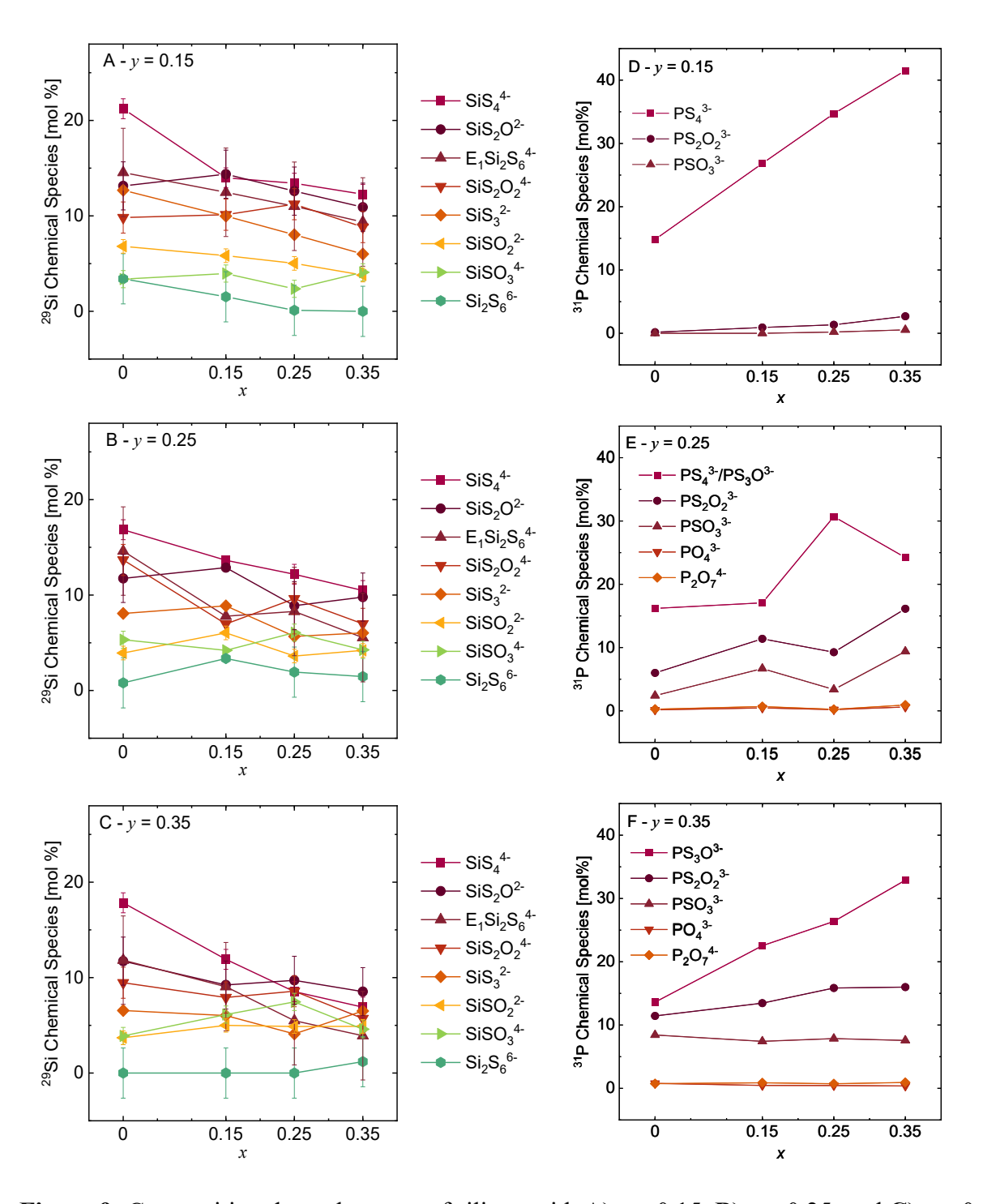


Figure 9: Composition dependence, x, of silicon with A) y = 0.15, B) y = 0.25, and C) y = 0.35, and phosphorus with D) y = 0.15, E) y = 0.25, and F) y = 0.35 chemical species for all

GSEs in the (0.6-0.08y)Na₂S + (0.4+0.08y)[(1-y)[(1-x)SiS₂+xPS_{5/2}]+yNaPO₃] (NaPSiSO) series. In these plots, for any one composition, the sum of all of the mol % values for both the Si and P SRO species is 100%.

Due to the high modifier content in these GSEs, R = 3, where R = [Na]/([Si] + [P]), the preponderance of the various SRO species has large numbers of NBO and NBSs. It is noted that the terminal P^0 SRO group has R = 3, whereas the terminal Si SRO group has R = 4. Now that all the fractions of all of the various SRO groups in these GSEs are known, the overall fractions of BS, BO, NBS, and NBO can be determined, and these are shown in **Figures 10A-B.** As expected from the high R-value for these glasses, most of the oxygen and sulfur are in the form of NBO and NBS, respectively. **Figure 10A** shows that the fractions of the NBOs and BOs more strongly depend upon y, but are nearly independent of x, where the fractions of NBO and NBS increase with increasing y. **Figure 10B** shows that the relatively high NBS fractions and the relatively low BS fractions are essentially independent of y, but do increase and decrease, respectively with x, the amount of PS_{5/2} in the GSEs.

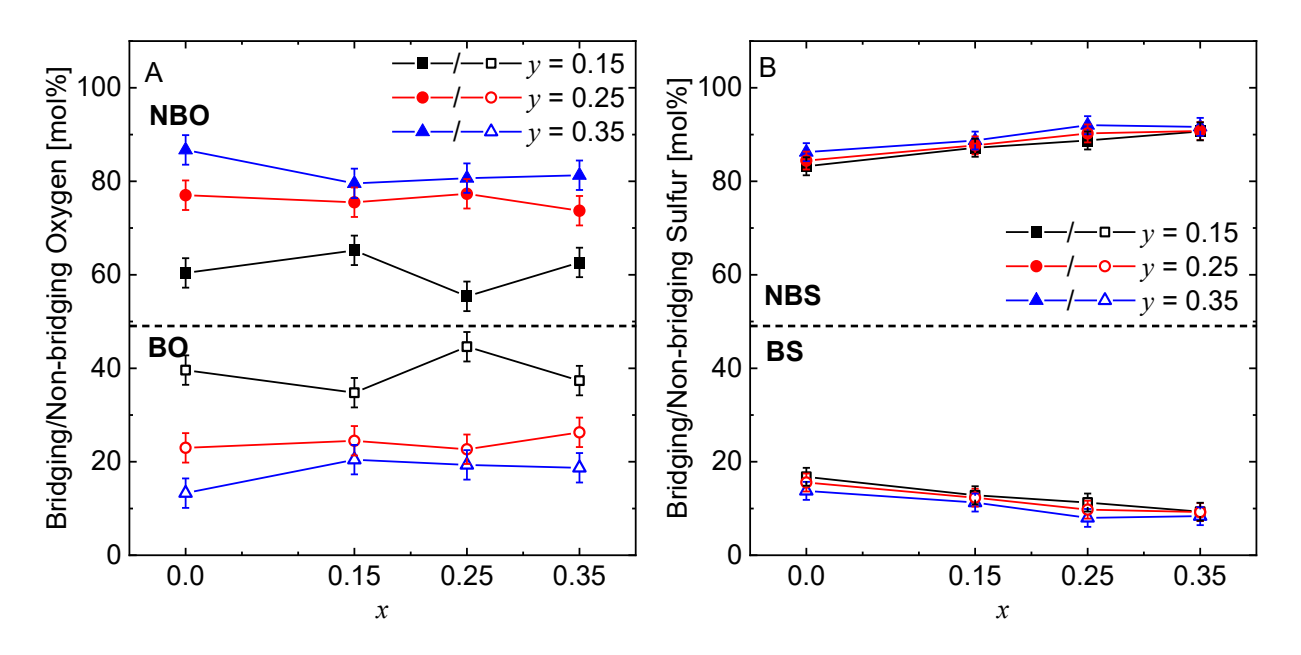


Figure 10: A) Bridging oxygen (BO) (bottom) and non-bridging oxygen (NBO) (top), **B)** bridging sulfur (BS) (bottom) and non-bridging sulfur (NBS) (top) for all the glasses in the (0.6-0.08y)Na₂S + (0.4+0.08y)[(1-y)[(1-y)SiS₂+xPS_{5/2}]+yNaPO₃] (NaPSiSO) series.

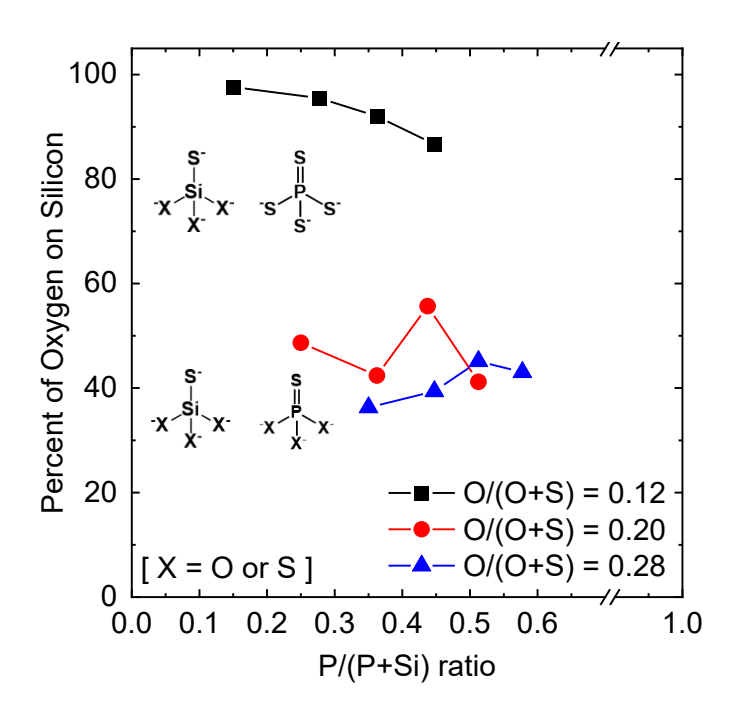


Figure 11: The percentage of oxygen bonded to silicon tetrahedra as a function of the fraction of phosphorus in the GSEs. At low oxygen concentrations, black symbols, almost 100 % of the oxygen are bonded to silicon tetrahedra. As the concentration of oxygen increases, red and blue symbols, the oxygen bonds more equally to the silicon and phosphorus tetrahedra.

Interestingly, at low concentrations of oxygen, silicon coordinates with almost 100% of the oxygen, **Figure 11**. At higher concentrations of oxygen, however, the oxygen is equally shared between the glass formers, silicon and phosphorus. Generally, the much more negative Gibb's Free-Energy of formation of silicates compared to phosphates, $\Delta G^{\circ}_{formation}(SiO_2, 298K) = -205 \text{ kJ}$ mol⁻¹ compared to $\Delta G^{\circ}_{formation}(PO_{5/2}, 298k) = -161 \text{ kJ mol}^{-1},^{51}$ explains the preferential bonding of oxygen (~95%) with silicon at low concentrations of oxygen, O/(O+S) = 0.12. However, and perhaps unexpectedly, as the concentration of oxygen increases, O/(O+S) = 0.20 and O/(O+S) = 0.28, oxygen is distributed to silicon and phosphorus more uniformly, **Figure 11**. Due to this inconsistency, the reaction energies of the precursors Na₂S, PS_{5/2}, SiS₂, and NaPO₃ to create the various end product SRO species were determined and used to investigate the most favorable

reaction pathways.⁵²⁻⁵³ This method and various inputs into the calculations are shown in Table S6.

The reaction energies for the formation of the observed SRO species was identified with the series of reactions shown in Table 1, where each row depicts Reaction Schema 1-7.54-56 The most energetically favorable reaction, Reaction Scheme 1, is the formation of Na₃PS₄ from Na₂S and P₂S₅. Therefore, P₂S₅ and its compounds are expected to be the first to consume Na₂S. This is consistent with the NMR analysis, where the P⁰ SRO unit, Na₃PS₄, was determined to be present in all of the GSEs reported here, Figure 9B. The second most favorable reaction pathway was the anion exchange reaction between SiS₂ and NaPO₃, Reaction Scheme 2. In this process, SiS₂ and NaPO₃ react and NaPS₃ and SiO₂ form. While this may not be the final product, it suggests a high affinity for oxygen-silicon bonding. Furthermore, this allows for even more Na₃PS₄ to form as the third most favorable reaction, Equation 3, which shows the formation of Na₃PS₄ from Na₂S and NaPS₃. SiO₂ can then react and form the MOS networking and non-networking species seen in the MAS NMR spectra, Figure 9B, while the remaining unreacted SiS₂ can form various thio-silicates, Equation 4-5. Therefore, at low concentrations of NaPO₃ and high concentrations of silicon, low y, there is an energetic driving force for anion exchange where silicon extracts oxygen from the NaPO₃ and in turn releases sulfur to bond to the phosphorus.

At higher concentrations of NaPO₃, higher y, there becomes a limited concentration of remaining Na₂S within the system due to the more favorable occurrence of the pathways shown in **Reaction Schema 1-5**. This results in a series of competing reactions occurring until all the precursors are consumed and the system achieves charge neutrality **Reaction Schema 6-8**. Therefore, we see not only the pure sulfide P^0 SRO structures, but also the MOS P^0 species.

Table 1: Tabulated reaction energies for precursors used in the synthesis of these NaPSiSO GSEs. Calculated via the mixed GGA/GGA+U/R2SCAN functionals via the Materials Project API. 55

Reaction Scheme	Reactants	Product(s)	Reaction Energy (kJ mol ⁻¹)
1	$3 \text{ Na}_2\text{S} + \text{P}_2\text{S}_5$	2 Na ₃ PS ₄	-80.2
2	$3 \operatorname{SiS}_2 + 2 \operatorname{NaPO}_3$	$2 \text{ NaPS}_3 + 3 \text{ SiO}_2$	-50.2
3	$Na_2S + NaPS_3$	Na ₃ PS ₄	-47.0
4	$2 \text{ Na}_2\text{S} + \text{SiS}_2$	Na ₄ SiS ₄	-37.9
<mark>5</mark>	$Na_2S + SiS_2$	Na ₂ Si ₂ S ₅	-31.9
<mark>6</mark>	$Na_2S + NaPO_3$	Na ₃ PSO ₃	-33.0
7	$3 \text{ Na}_2\text{S} + 5 \text{ NaPO}_3$	$Na_3PS_3O + 2 Na_4P_2O_7$	-30.5
8	$2 \text{ Na}_2\text{S} + 3 \text{ NaPO}_3$	$Na_3P(SO)_2 + Na_4P_2O_7$	-31.0

Physical Properties of NaPSiSO GSEs

The densities and moduli, necessary parameters to model the conductivity activation energies, see below, were found to be highly dependent on the concentration of oxygen.⁵⁷ To present these dependencies, the O/(O+S) ratio was held constant while the P/(P+Si) ratio was varied, **Figures 12A-B**. The densities are within a range of ~ 2.06 to 2.16 g cm⁻³, expectedly lower than the density of soda lime glass, ~ 2.5 g cm⁻³, and within the expected range of similar sulfide GSEs seen in literature.⁵⁸⁻⁵⁹ Watson *et al.*, for example, reported values of ~ 2.05 g cm⁻³ in the pure sulfide Na₂S-SiS₂-PS_{5/2} GSE system.⁵⁸ The range of density values determined for the MOS NaPSiSO glasses reported here are higher and increase with the concentration of oxygen, **Figure 12A**. This trend is consistent with the slight decrease in molar volume, V_m , with increasing oxygen, **Figure 12C**, and trends observed in other MOS GSEs. For example, the Na₄P₂S_{7-x}O_x series reported by Kmiec *et al.* showed an increase in density and corresponding decrease in molar

volume with increasing x.²² These NaPSiSO GSEs show Young's moduli that are comparable to other pure sulfide GSEs and are on the order of 20 GPa and higher.^{22, 60} In **Figure 12C**, as the concentration of oxygen increases, so do the moduli. Despite the increase in non-networking P⁰ SRO species with increasing phosphorus, **Figure 9A**, there is no decrease in the density and moduli, **Figure 12C**. Added oxygen, even when 50% of it is bonded to non-networking P⁰ species, **Figure 11**, increases the density and modulii of GSE in this system, **Figure 12C**.

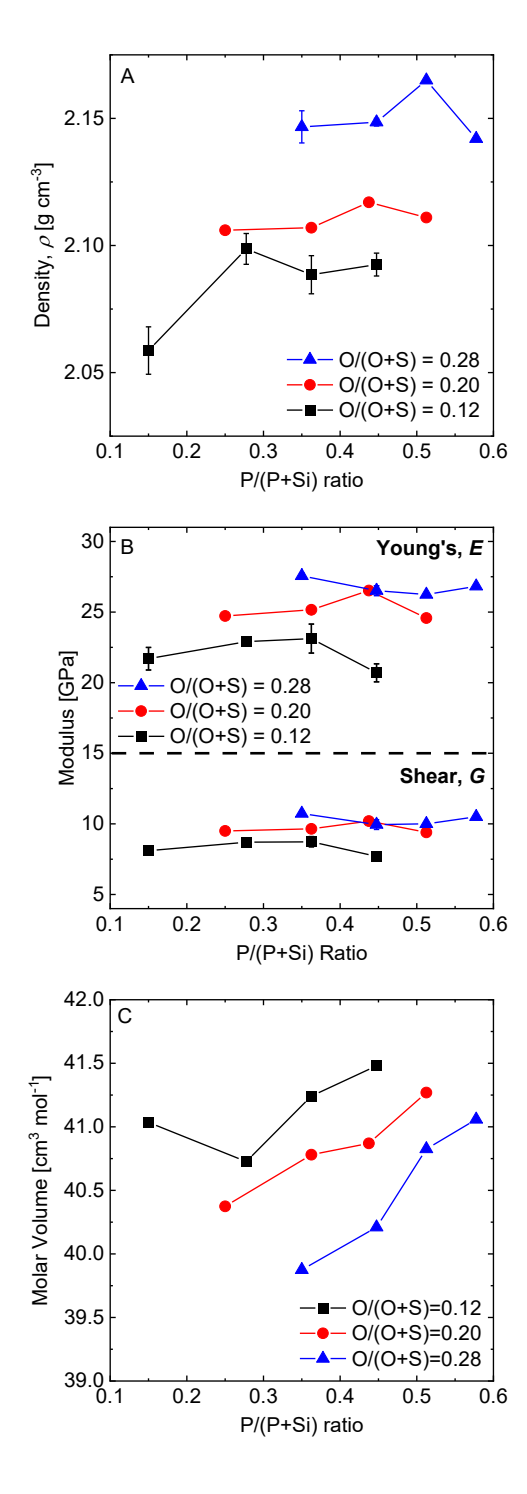


Figure 12: A) Density, ρ , **B)** Young's, E (top), and shear, G (bottom), modulus, **C)** and the molar volume, V_m of GSEs in the $(0.6\text{-}0.08y)\text{Na}_2\text{S} + (0.4\text{+}0.08y)[(1\text{-}y)[(1\text{-}x)\text{SiS}_2+x\text{PS}_{5/2}]+y\text{NaPO}_3]}$ (NaPSiSO) series plotted in groups of their O/(O+S) molar ratios as a function of their variable P/(P+Si) ratios.

Sodium Ion Conductivity

Similar to the large changes exhibited by the T_g 's, the changes in the conductivity span over an order of magnitude. For example, compare the highest to the lowest conductivity samples: the sample with x = 0.0, y = 0.15 where $\sigma_{d.c.}(75 \,^{\circ}\text{C}) = 4.23 \, \text{x} \, 10^{-4} \, (\Omega \text{cm})^{-1}$ versus the sample with x = 0.35, $y = 0.35 \, \sigma_{d.c.}(75 \,^{\circ}\text{C}) = 2.75 \, \text{x} \, 10^{-5} \, (\Omega \text{cm})^{-1}$. **Figure 13A** shows the combined effects of oxygen and phosphorus on the ionic conductivity, where the O/(O+S) ratio was held constant while the P/(P+Si) ratio was varied. Added oxygen at constant phosphorus decreases the conductivity, as does added phosphorus at constant oxygen.

The decrease in the conductivity with added oxygen is consistent with the general trends of more poorly conducting oxide glasses. The trend of decreasing conductivity with increasing phosphorous is consistent with the trend observed by Martin *et al.*⁶¹ Due to the P⁺⁵ valency, the many phosphorus SRO units carry less charge for the four bonding atoms, oxygen and sulfur, than silicon at the same R value for the glass. For example, at R = 3, Na₃PS₄ has four bonded sulfur atoms and their associated volumes. While at R = 3 for Na₃SiS₃S_{1/2}, there are only 3.5, on average, bonded sulfur atoms. Hence, the sodium cation density is higher for silicon SRO structures leading to shorter cation jump distances, see below, for the silicon rich GSEs and longer cation jump distances as silicon is replaced by phosphorus. This is shown in **Figure 14A** where the conductivity is extrapolated out to 100% phosphorus for the Na₃P₃S_{3.4}O_{0.6}, which has a comparable oxygen to sulfur ratio of, 0.15, compared to the 0.12 ratio of the GSEs reported here. These effects will be examined in more detail below where the conductivity activation energies are modeled.

Despite the relatively small changes in the moduli and density of the GSEs in the NaPSiSO series, there are significant changes in the T_g of the NaPSiSO GSEs. Across the series, there is a change in the T_g by over 100 °C; see the x = 0.0, y = 0.15 ($T_g = 322$ °C) sample compared to the x = 0.35, y = 0.35 ($T_g = 215$ °C) sample, **Figure 1B**. **Figure 13C** presents the T_g 's as a function of

the percent phosphorus out of the total glass former, P/(P+Si) ratio, in groups on the percent oxygen out of the total anion concentration, O/(O+S) ratio. The NaPSiSO MOS system reported here exhibits a linear decrease in the T_g with added phosphorus, **Figure 13C**, independent of oxygen. The phosphorus is found in essentially fully P^0 SRO units, 100 % non-networking, and this is consistent with the compositional R-value = 3 for these GSEs, **Figure 9A**. Thus, the observed decrease in the T_g is not only independent of the coordination of oxygen on these phosphorus tetrahedra, but also is consistent with a decrease in networking SRO structures; simply, an increase in the concentration of phosphorus SRO units. The decrease in T_g to almost 200 °C is consistent with other phosphate glass systems; for example, the Na₃PS_{4-x}O_x and Na₄P₂S_{7-x}O_x GSE systems, with R-values of 3 and 2, respectively, both have T_g values below 200 °C, despite the latter series being more highly networked. 10,62

Figure 13B shows that the conductivity activation energies increase with both the P/(P+Si)) and O/(O+S) ratios. However, the activation energies decrease linearly with T_g and are essentially independent of the O/(O+S) ratio, Figure 13D. To understand these relationships, it is important to note that the structure of these invert glasses is comprised of isolated monomeric and dimer anionic SRO species. Without a long-range, polymeric network, as is expected in covalent glasses, the ionic interactions (non-bridging species) among the sodium ions and the anionic SRO species dictate the average bonding strength affecting both the properties and the ion conduction mechanisms. From the NMR analysis shown in Figure 10 and discussed above, the incorporated oxygen and sulfur were found to reside primarily on non-networking phosphorus and silicon SRO species, leading to an increase in the ionic bond strength while decreasing the degree of covalency in the glass structure. Surprisingly, while these findings are unique in the family of MOS glasses, they are in good agreement with correlations found in many oxide glasses.

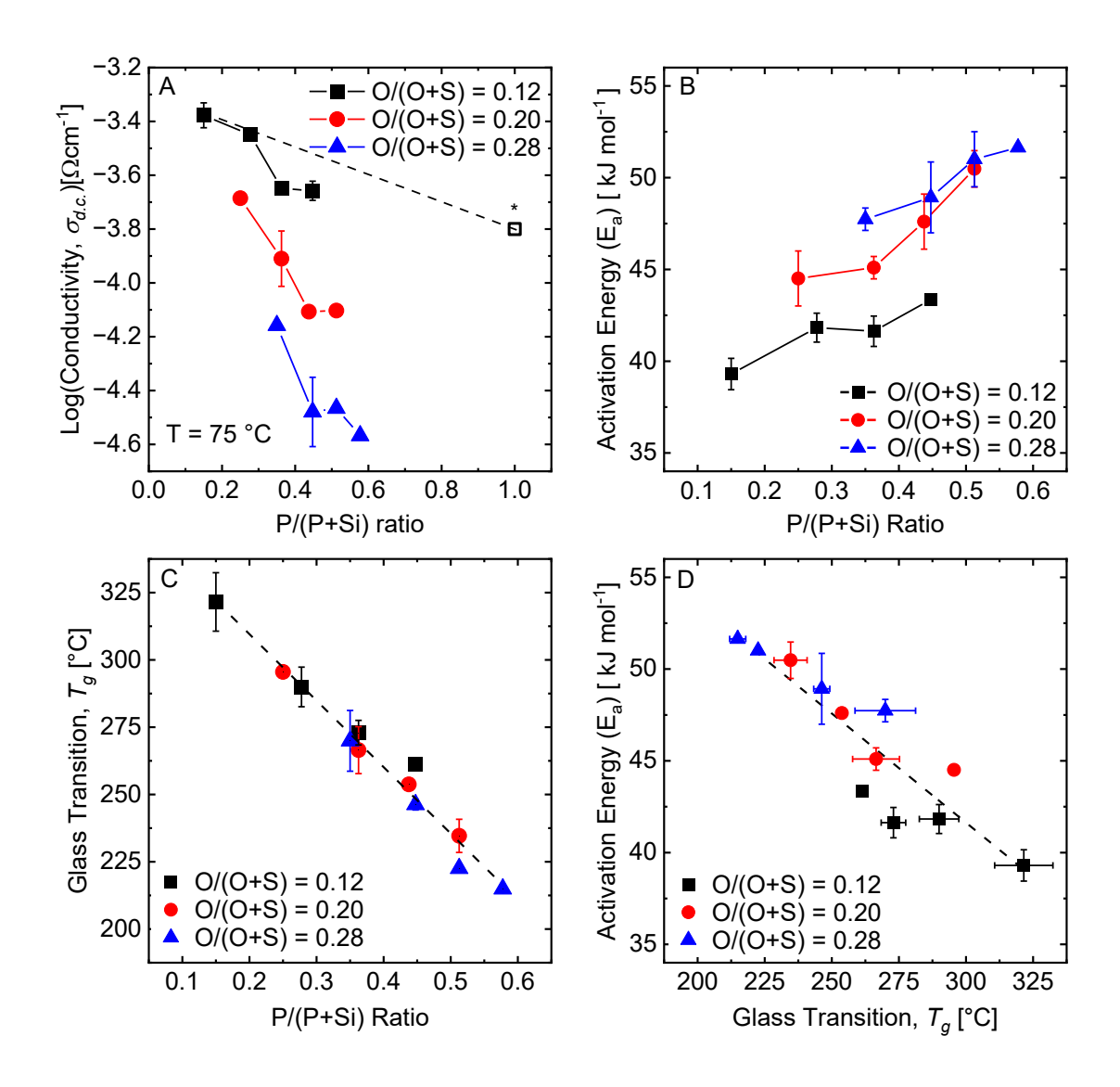


Figure 13: A) Ionic conductivity, **B)** conductivity-activation energies, and **C)** glass transition temperatures, T_g 's, of GSEs in the (0.6-0.08y)Na₂S + (0.4+0.08y)[(1-y)[(1-x)SiS₂+xPS_{5/2}]+yNaPO₃] (NaPSiSO) series plotted in groups of their O/(O+S) molar ratios as a function of the variable P/(P+Si) ratio. **D)** Activation energies from **B** plotted against the T_g 's from **C**. *Conductivity at 75 °C of Na₃PS_{3.4}O_{0.6}, where P/(P+Si) =1, is taken from Chi *et al.* ¹⁰

The effects of added oxygen on the ionic conductivity and activation energy are shown in **Figures 14A-B**, where the conductivities and activation energies of groups of GSEs with similar P/(P+Si) ratios, 0.36 and 0.44, are plotted as a function of their O/(O+S) ratios. Like many other MOS GSEs reported in the literature, small concentrations of added oxygen increase the ionic conductivity, **Figure 14A**. ^{10, 13, 38} The pure sulfide GSE, NaPSiS, having no MOS species, has a

smaller free volume compared to the NaPSiSO GSEs, **Figure 14C**. The formation of MOS anion P^0 , Si^0 , and Si^2 species appear to increase the free-volume, allowing more space for ionic motion at low oxygen concentrations, **Figure 14C**. Up to an O/(O+S) molar ratio of 0.2, the conductivity increases before decreasing, where the free-volume maximizes and the coulombic binding energy term of the total activation energy, see below, increases with higher concentrations of $PS_2O_2^{3-}$ and PSO_3^{3-} anions, **Figure 14B**, for the P/(P+Si) = 0.36 GSEs. The P/(P+Si) = 0.44 GSEs appear to show no such maximum in the free-volume.

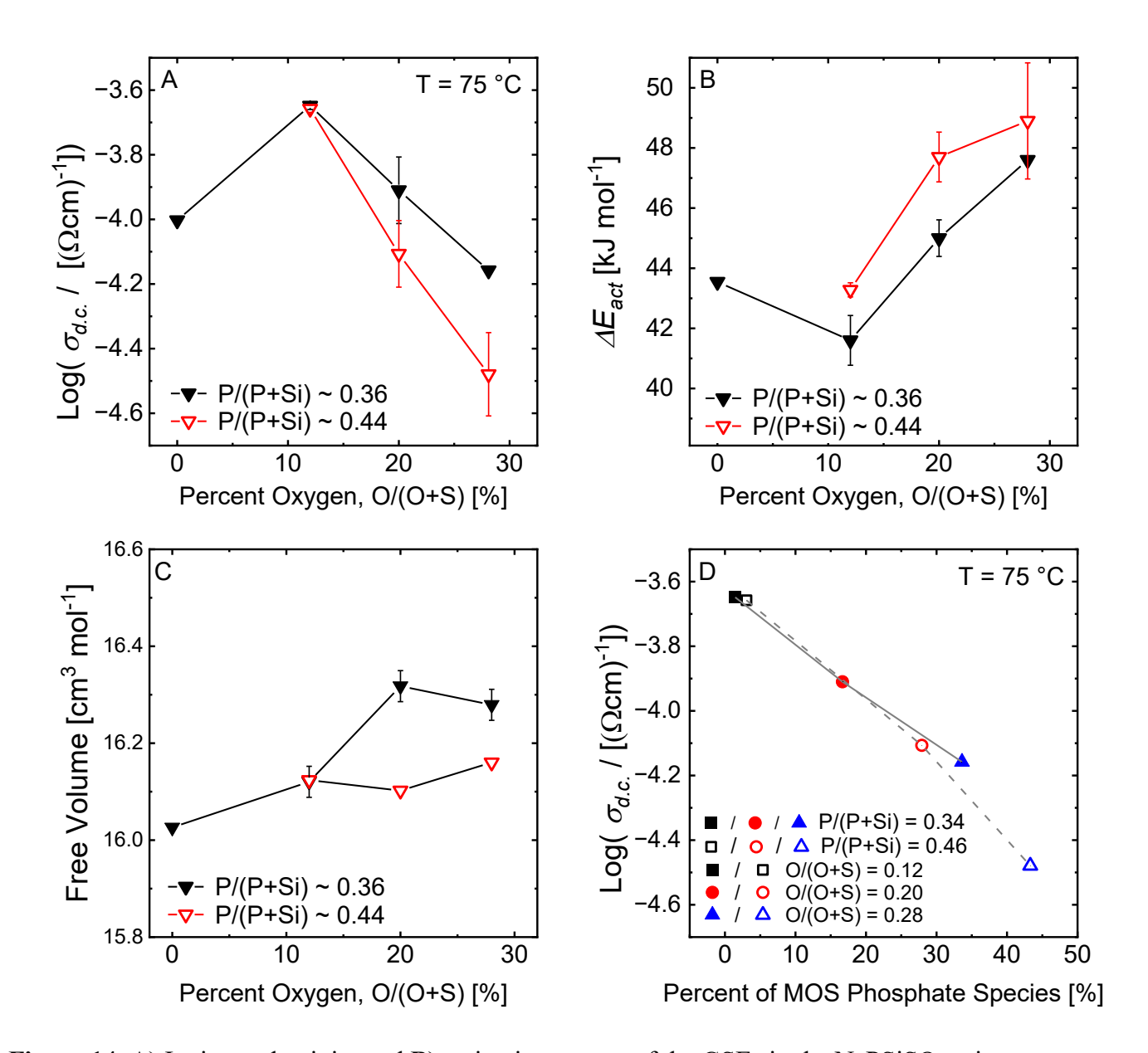


Figure 14: A) Ionic conductivity and B) activation energy of the GSEs in the NaPSiSO series plotted in groups of their P/(P+Si) ratios as a function of the O/(O+S) ratio. While the y = 0 pure sulfide GSEs were not prepared as a part of the NaPSiSO series, this one was synthesized for comparison purposes such that some of the MOS GSEs could be compared to a pure sulfide GSE. C) The calculated free volume of each glass in A-B.

D) Ionic conductivity of the NaPSiSO GSE as a function of the percentage of MOS phosphate SRO species (PS₃O³⁻, PS₂O₂³⁻, PSO₃³⁻) for NaPSiSO GSEs from graph A. The specific percent of phosphorus and oxygen are identified for each glass in the legend.

Oxygen has a profound impact on the conductivity of these GSEs, particularly with respect to its coordination around phosphorus. As shown in **Figure 14D**, the conductivities of the samples

from **Figure 14A** are replotted as a function of the percent of the MOS phosphate SRO species. This graph shows the impact of increased oxygen surrounding phosphorus SRO species. At low concentrations of oxygen, where there are almost no MOS phosphate species, the conductivity is relatively unchanged despite the 35% increase in the concentration of phosphorus; note the square symbols. However, as the concentration of oxygen increases and oxygen coordinates more prominently around phosphorus SRO species, the conductivity decreases systematically.

Finally, considering a conductivity of 10^{-5} (Ω cm)⁻¹ at room temperature as a minimum metric for competitive SSEs for use in sodium ASSBs, only the y = 0.15 GSEs in the NaPSiSO series meets this requirement, which has a concentration of only ~ 4 mol% oxygen. At higher concentrations of oxygen, the conductivity may become too low, especially at 25 °C, for many battery applications. At low oxygen concentrations, the oxygen is found primarily in BO Si-O-Si sites due to the higher field strength of the oxygen anion and the more negative Gibb's free-energy of formation of alkali silicates compared to alkali phosphates. However, as described above, at high oxygen contents, this favorable Gibb's Free-Energy for oxide silicates over oxide phosphates is lost and oxygen equally shares with the phosphorus centers forcing it to NBO sites. Therefore, when oxygen occupies covalent BO sites, the ionic conductivity remains high; however, when oxygen bonds in ionic NBO sites, these act as sodium ion trapping sites and decrease the conductivity.

CMAS Model for Conductivity Activation Energy

To investigate further the combined effects of mixing the anions, oxygen and sulfur, and mixing the glass forming cations, phosphorus and silicon, on the ionic conductivity, we next investigate the dominant factor controlling the composition dependence of the sodium ion conductivity, that is the conductivity activation energies. The conductivity activation energies in

these GSEs were modeled using the Christensen-Martin-Anderson-Stuart (CMAS) model, first presented by Christensen *et al.*⁶⁴ This model has addressed many of the short comings of the original Anderson Stuart description of the activation energy for ionic conduction in glasses.⁶⁵ The activation energies for each glass in the NaPSiSO series were calculated using the CMAS model to check the agreement between the experimentally determined values for the activation energy. The CMAS model for the total activation energy, ΔE_{CMAS} in kJ mol⁻¹, is taken as the sum of the strain energy, ΔE_S , and the binding energy, ΔE_B , **Equation 8**. The ΔE_S is defined as the energy required for a sodium ion to mechanically strain the lattice and jump to an adjacent site, **Equation 9**, while the ΔE_B is the electrostatic binding energy that is needed to generate mobile charge carriers, **Equation 11**.

(8)
$$\Delta E_{CMAS} = \Delta E_S + \Delta E_B$$

(9)
$$\Delta E_S = \pi G \left(\frac{\lambda_{cation}}{2} \right) \left(r_{Na^+} - r_D \right)^2$$

$$\lambda_{cation} = 2 \left(\frac{V_m}{N_{Na} N_A} \right)^{1/3}$$

In Equation 9, G is the shear modulus, shown in Figure 2, in Pa, and r_{Na+} is the ionic radius of a mobile sodium ion in m. r_D is the doorway radius in m, approximated by fitting the composition dependence, O/(O+S), of the r_D values between pure sulfur tetrahedral sites, O/(O+S) = 0, and pure oxygen trigonal bipyramidal oxygen sites, O/(O+S) = 1, using a fourth order polynomial, see Figure S9.²² The cation jump distance, λ_{cation} in m, was approximated using a simple cubic model, which is defined in Equation 10, where V_m is the molar volume in m³ mol⁻¹, N_{Na} is the moles of sodium in one formula unit of glass, and N_A is Avogadro's number in mol⁻¹.

(11)
$$\Delta E_{B} = \frac{M_{C} Z_{Na} Z_{X} e^{2}}{4\pi \varepsilon_{0} \varepsilon_{\infty}} \left(\frac{1}{r_{Na^{+}} + r_{X^{-}}} - \frac{1}{r_{Na^{+}} + r_{X^{-}} + \frac{\lambda_{cation}}{2}} \right)$$

(12)
$$r_{Y^{-}} = f_{O}r_{O} + f_{S}r_{S}$$

In **Equation 11**, M_C is the Madelung constant, Z_{Na} and Z_X are the charges of the cation and anion, e is the charge in C of the electron, ε_0 is the permittivity of free-space in C^2 N⁻¹ m⁻², ε_∞ is the relative permittivity of the GSE, see **Figure 5B**, and r_X is the anion radius in m. Due to the MOS compositions in these NaPSiSO GSEs, r_X is composition dependent. In **Equation 12**, r_X was calculated using a weighted average of the anionic radii of oxygen and sulfur, r_O and r_S , respectively; where, f_O and f_S are the mole fractions of oxygen and sulfur, respectively, in each of the GSEs. **Table S7** provides all the values and parameters used to in the CMAS calculations.

From Equations 9 and 11, the only unknown parameter is M_C which can only be modelled in glassy solids, though needed to apply Equation 8 to the GSEs reported here. With this in mind, $\Delta E_B/M_C$ and ΔE_S values were calculated from the known values described above. Figure 15A shows ΔE_S values between 1.4 and 2.2 kJ mol⁻¹, which agree well with the literature of similar ion conducting glasses.^{22, 64-65} Similarly, Figure 15B shows the values for $\Delta E_B/M_C$ in these high modifier, high conductivity GSEs, which are expectedly lower than those of high activation energy oxide glasses and lower than those of less highly optimized and lower conductivity pure sulfide glasses.^{64, 66} Additionally, the ΔE_S and $\Delta E_B/M_C$ values show an expected trend with composition, where as oxygen increases in the glass (increasing y), the permittivity decreases and the doorway radius decreases, leading to each part of the total activation to increase. The values of $\Delta E_B/M_C$ and ΔE_S along with the experimental value ΔE_{act} can be used to calculate M_C through Equation 13 and are shown in Figure 15D.

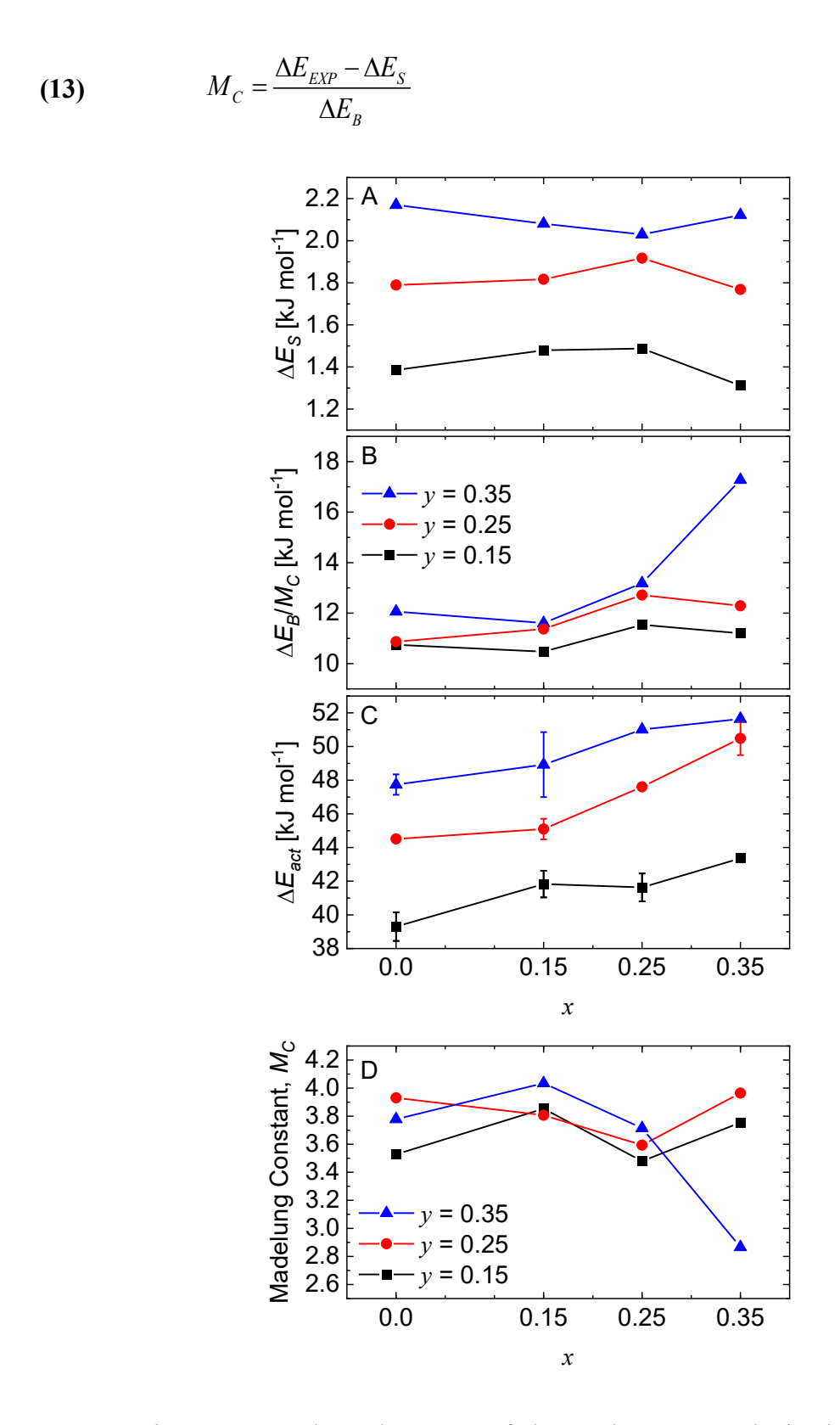


Figure 15: A) The ΔE_S B) and $\Delta E_B/M_C$ parts of the total C) ΔE_{act} obtained from Arrhenius conductivity plots, Figure 3, as well as the calculated D) M_C derived from Equation

11 for all GSEs in the (0.6-0.08y)Na₂S + (0.4+0.08y)[(1-y)][(1-x)SiS₂+xPS_{5/2}]+yNaPO₃] (NaPSiSO) series.

The calculated values for the lattice-constant-based, charge compensated Madelung constant, M_C , agree well with the literature values for NaCl, which is reported as 3.49.⁶⁷⁻⁶⁸ The value is calculated using a fixed lattice constant, rather than the more commonly used nearest neighbor distance. Using a lattice constant is more consistent with the random network theory used to model glass, where the sodium ions are assumed to be evenly distributed throughout the glass network due to like-charge repulsion.⁶⁹ Due to the lack of long-range order, this approach is well-suited to apply to the GSE system reported here and is in good agreement with the simple cubic model for calculating the jump distance, **Equation 10** and **Figure 15D**.⁶⁷⁻⁶⁸ Overall, the value of 3.49 calculated for NaCl using the fixed lattice spacing is consistent with the values reported here and the model follows the expected trends, **Figure 15**, validating the reported values for the conductivity-activation energies.

Conclusions

In conclusion, the NaPSiSO GSEs investigated here were found exhibit among the highest yet reported sodium ion conductivities for any GSE and reach $\sim 2.5 \times 10^{-4} \, (\Omega \text{cm})^{-1}$ at 75 °C, an expected application temperature. As found in other MOS GSEs, the conductivity exhibits a maximum value at low oxygen additions and this has been ascribed to a maximum in the free-volume of the glass. The free-volume maximum is associated with a maximum in the number of BOs. Thereafter, the conductivity decreases with further oxygen additions as the oxygens convert to ionic non-bridging oxygens that serve as more stable deep energy well traps for sodium. The SRO structures of these MGF MOS GSEs were investigated using 29 Si and 31 P MAS NMR spectra, which showed a predominance of Si⁰ and Si² and non-networking, P⁰ sulfide and MOS chemical species. The activation energies for sodium ion conduction as well as the mechanical properties

and densities were affected strongly by the concentration of oxygen in these MGF MOS GSEs. Contrastingly, the T_g values of these glasses were independent of oxygen and decreased exclusively due to increasing phosphorus, which plasticized the glass network due to its nonnetworking P^0 structure. The conductivities were dependent both on added phosphorus and oxygen, evident not only in the effect of oxygen on the activation energies, but also when compared to pure phosphate glass with similar O/S ratio. The coulombic force from oxygen as well as the resonance from the double bond on the phosphorous tetrahedra created a stronger activation energy for sodium ion conduction. Although this glass series does not report a complete spectrum of P/(P+Si) percentages, from 0 to 100%, this work does report a linear trend in properties when silicon is substituted for phosphorus. Future work will include further glasses in this compositional series to solidify a potential MGF effect. In addition, the resistance to crystallization observed in this compositional series will be further investigated and related to the sulfur impurities present in each composition.

Supporting Information

The following Supporting Information is available from the corresponding author upon request.

Figure S1: XRD of select NaPSiSO samples.

Figure S2: Supplementary Arrhenius conductivity plots.

Figure S3: Example $ln(\sigma T)$ plot for reference.

Figure S4: Conductivity at high, intermediate, and low temperatures for all NaPSiSO samples.

Figure S5: Raman of all the NaPSiSO samples compared to a sulfide sample.

Figure S6: Sulfur impurity calculation for all NaPSiSO samples.

Figure S7: Comparison of spinning side bands of three ³¹P MAS NMR spectra.

Figure S8: All NMR deconvolutions.

Figure S9: Polynomial used to fit doorway radius, r_D .

Figure S10: ³¹P and ²⁹Si MAS NMR spectra of a pure sulfide NaPSiS GSE.

Table S1: Summary of compositions.

Table S2: Summary of sound velocity measurements and moduli calculations.

Table S3: Structural depictions of SRO species in NaPSiSO samples.

Table S4: Summary of parameters used to fit ³¹P MAS NMR spectra.

Table S5: Summary of parameters used to fit ²⁹Si MAS NMR spectra.

Table S6: Summary of data used for most favorable reaction determinations.

Table S7: Summary of parameters used to apply CMAS model.

Acknowledgements

The work at ISU was supported by the Iowa Energy Center of the Iowa Department of Economic Development through grant number 307352, by the National Science Foundation through grants DMR 1936913 and 217445, and by the ARPA-E of the Department of Energy through contract numbers DE-AR0000654 and DE-AR-0000778. Additional funding for this work was provided by the Vehicle Technology Office within the Department of Energy though contract DE-EE0008852. The MAS NMR spectroscopy and reaction energy calculations work at the University of Texas at Austin was supported by the U.S. Department of Energy, Office of Basic Energy Sciences, Division of Materials Science and Engineering under award number DE-SC0005397.

References

- 1. Gond, R.; van Ekeren, W.; Mogensen, R.; Naylor, A. J.; Younesi, R., Non-flammable liquid electrolytes for safe batteries. *Mater Horiz* **2021**, *8* (11), 2913-2928.
- 2. Jia, Y.; Li, J.; Yuan, C.; Gao, X.; Yao, W.; Lee, M.; Xu, J., Data-driven safety risk prediction of lithium-ion battery. *Advanced Energy Materials* **2021**, *11* (18).

- 3. Ferrari, S.; Falco, M.; Muñoz-García, A. B.; Bonomo, M.; Brutti, S.; Pavone, M.; Gerbaldi, C., Solid-state post li metal ion batteries: A sustainable forthcoming reality? *Advanced Energy Materials* **2021,** *11* (43).
- 4. Lee, S.; Manthiram, A., Can cobalt be eliminated from lithium-ion batteries? *ACS Energy Letters* **2022,** *7* (9), 3058-3063.
- 5. Hirsh, H. S.; Li, Y. X.; Tan, D. H. S.; Zhang, M. H.; Zhao, E. Y.; Meng, Y. S., Sodium-ion batteries paving the way for grid energy storage. *Advanced Energy Materials* **2020**, *10* (32).
- 6. Komaba, S., Sodium-driven rechargeable batteries: An effort towards future energy storage. *Chemistry Letters* **2020**, *49* (12), 1507-1516.
- 7. Yang, Z.; Tang, B.; Xie, Z.; Zhou, Z., Nasicon-type na3zr2si2po12 solid-state electrolytes for sodium batteries**. *ChemElectroChem* **2021**, *8* (6), 1035-1047.
- 8. Fertig, M. P.; Skadell, K.; Schulz, M.; Dirksen, C.; Adelhelm, P.; Stelter, M., From high- to low-temperature: The revival of sodium-beta alumina for sodium solid-state batteries. *Batteries & Supercaps* **2021**, *5* (1).
- 9. Wang, Z.; Ma, J.; Cui, P.; Yao, X., High-rate solid polymer electrolyte based flexible all-solid-state lithium metal batteries. *ACS Appl Mater Interfaces* **2022**, *14* (30), 34649-34655.
- 10. Chi, X.; Zhang, Y.; Hao, F.; Kmiec, S.; Dong, H.; Xu, R.; Zhao, K.; Ai, Q.; Terlier, T.; Wang, L.; Zhao, L.; Guo, L.; Lou, J.; Xin, H. L.; Martin, S. W.; Yao, Y., An electrochemically stable homogeneous glassy electrolyte formed at room temperature for all-solid-state sodium batteries. *Nat Commun* **2022**, *13* (1), 2854.
- 11. Tsukasaki, H.; Morimoto, H.; Mori, S., Ionic conductivity and thermal stability of li2o–li2s–p2s5 oxysulfide glass. *Solid State Ionics* **2020**, *347*.
- 12. Kim, K. J.; Balaish, M.; Wadaguchi, M.; Kong, L.; Rupp, J. L. M., Solid-state li-metal batteries: Challenges and horizons of oxide and sulfide solid electrolytes and their interfaces. *Advanced Energy Materials* **2020**, *11* (1).
- 13. Cengiz, M.; Oh, H.; Lee, S.-H., Lithium dendrite growth suppression and ionic conductivity of li2s-p2s5-p2o5 glass solid electrolytes prepared by mechanical milling. *Journal of The Electrochemical Society* **2019**, *166* (16), A3997-A4004.
- 14. Raguenet, B.; Tricot, G.; Silly, G.; Ribes, M.; Pradel, A., Revisiting the 'mixed glass former effect' in ultra-fast quenched borophosphate glasses by advanced 1d/2d solid state nmr. *Journal of Materials Chemistry* **2011**, *21* (44), 17693-17704.
- 15. Olson, M.; Kmiec, S.; Martin, S. W., Napon doping of na(4)p(2)s(7) glass and its effects on the structure and properties of mixed oxy-sulfide-nitride phosphate glass. *Inorg Chem* **2022**, *61* (44), 17469-17484.
- 16. De Souza, J. E.; Rojas De Souza, S.; Gebhardt, R.; Kmiec, S.; Whale, A.; Warthen Martin, S., Lipon and napon glasses: A study of the ammonolysis of lithium and sodium metaphosphate melts. *International Journal of Applied Glass Science* **2019**, *11* (1), 78-86.
- 17. Pershina, S. V.; Kuznetsova, T. A.; Vovkotrub, E. G.; Belyakov, S. A.; Kuznetsova, E. S., Solid electrolyte membranes based on li(2)o-al(2)o(3)-geo(2)-sio(2)-p(2)o(5) glasses for all-solid state batteries. *Membranes (Basel)* **2022**, *12* (12).
- 18. Zhang, J.; Gao, C.; He, C.; Tan, L.; Kang, S.; Jiao, Q.; Xu, T.; Lin, C., Effects of different glass formers on li2s–p2s5–ms2(m = si, ge, sn) chalcogenide solid-state electrolytes. *Journal of the American Ceramic Society* **2022**, *106* (1), 354-364.
- 19. Zhao, R.; Hu, G.; Kmiec, S.; Wheaton, J.; Torres, V. M.; Martin, S. W., Grain-boundary-free glassy solid electrolytes based on sulfide materials: Effects of oxygen and nitrogen doping on electrochemical performance. *Batteries & Supercaps* **2022**, *5* (11).
- 20. Shastri, A.; Watson, D.; Ding, Q.-P.; Furukawa, Y.; Martin, S. W., 23na nuclear magnetic resonance study of yna2s +(1-y)[xsis2+(1-x)ps5/2] glassy solid electrolytes. *Solid State Ionics* **2019**, 340.

- 21. Tatsumisago, M.; Hirai, K.; Minami, T.; Takada, K.; Kondo, S., Superionic conduction in rapidly quenched li₂s-sis₂-li₃po₄ glasses. *Journal of the Ceramic Society of Japan* **1993**, *101* (1179), 1315-1317.
- 22. Kmiec, S.; Olson, M.; Kenney, M.; Martin, S. W., Interpretation of the na+ ionic conductivity in na4p2s7–xox mixed oxy-sulfide glasses: Effects of oxygen doping. *Chemistry of Materials* **2022**, *34* (21), 9479-9491.
- 23. Harris, R. K.; Becker, E. D.; Cabral de Menezes, S. M.; Granger, P.; Hoffman, R. E.; Zilm, K. W., Further conventions for nmr shielding and chemical shifts (iupac recommendations 2008). *Pure and Applied Chemistry* **2008**, *80* (1), 59-84.
- 24. Sakka, S.; Mackenzie, J. D., Relation between apparent glass transition temperature and liquidus temperature for inorganic glasses. *Journal of Non-Crystalline Solids* **1971**, *6*, 145-162.
- 25. Sakuda, A.; Hayashi, A.; Takigawa, Y.; Higashi, K.; Tatsumisago, M., Evaluation of elastic modulus of li₂s-p₅ glassy solid electrolyte by ultrasonic sound velocity measurement and compression test. *Journal of the Ceramic Society of Japan* **2013**, *121* (1419), 946-949.
- 26. Martin, S. W. Fast ionic conduction in glass: Compositionally induced effects on transport properties in high alkali oxide glasses (volumes i and ii). Ph.D., Purdue University, Ann Arbor, 1986.
- 27. Martin, S. W., Chapter 14: Glass and glass-ceramic sulfide and oxy-sulfide solid electrolytes. 2015.
- 28. Ohtomo, T.; Mizuno, F.; Hayashi, A.; Tadanaga, K.; Tatsumisago, M., Mechanochemical synthesis of lithium ion conducting glasses and glass-ceramics in the system li
- s-p-s. Solid State Ionics 2005, 176 (31-34), 2349-2353.
- 29. Nguyen, H.; Banerjee, A.; Wang, X.; Tan, D.; Wu, E. A.; Doux, J.-M.; Stephens, R.; Verbist, G.; Meng, Y. S., Single-step synthesis of highly conductive na3ps4 solid electrolyte for sodium all solid-state batteries. *Journal of Power Sources* **2019**, *435*.
- 30. Uematsu, M.; Yubuchi, S.; Noi, K.; Sakuda, A.; Hayashi, A.; Tatsumisago, M., Preparation of na3ps4 electrolyte by liquid-phase process using ether. *Solid State Ionics* **2018**, *320*, 33-37.
- 31. Wolfgang Brocknera, B. J., Frank Menzela, Vidar Remi Jensenb, Martin Ystenesb, Vibrational spectra and ab initio quantum mechanical calculation of energy, geometry and vibrational frequencies of the oxothiophosphate ions p03s3-, po2s23- and pos33-. *Journal of Molecular Structure* **1993**.
- 32. Zhao, R.; Kmiec, S.; Hu, G.; Martin, S. W., Lithium thiosilicophosphate glassy solid electrolytes synthesized by high-energy ball-milling and melt-quenching: Improved suppression of lithium dendrite growth by si doping. *ACS Appl Mater Interfaces* **2020**, *12* (2), 2327-2337.
- 33. Han, X.; Yilin, T., Vibrational dynamics of si-s-se glassy system on ab initio calculation. *Chalcogenide Letters* **2016**, *13* (3), 97-104.
- 34. Tenhover, M.; Hazle, M. A.; Grasselli, R. K., Raman-effect studies of sixs1-xglasses. *Physical Review B* **1984**, *29* (12), 6732-6735.
- 35. El Jaroudi, O.; Picquenard, E.; Gobeltz, N.; Demortier, A.; Corset, J., Raman spectroscopy study of the reaction between sodium sulfide or disulfide and sulfur: Identity of the species formed in solid and liquid phases. *Inorg Chem* **1999**, *38* (12), 2917-2923.
- 36. Nikiforidis, G.; van de Sanden, M. C. M.; Tsampas, M. N., High and intermediate temperature sodium-sulfur batteries for energy storage: Development, challenges and perspectives. *RSC Adv* **2019**, *9* (10), 5649-5673.
- 37. Aotani, N.; Iwamoto, K.; Takada, K.; Kondo, S., Synthesis and electrochemical properties of lithium ion conductive glass, li3po4-li2s-sis2. *Solid State Ionics* **1994**, *68* (1-2), 35-39.
- 38. Kawakami, Y.; Ikuta, H.; Uchida, T.; Wakihara, M., Ionic conduction of lithium in li2s ☐ sis2 ☐ li4sio4 glass system. *Thermochimica Acta* **1997**, *299* (1-2), 7-12.
- 39. Silva, A. M. B.; Queiroz, C. M.; Agathopoulos, S.; Correia, R. N.; Fernandes, M. H. V.; Oliveira, J. M., Structure of sio2–mgo–na2o glasses by ftir, raman and 29si mas nmr. *Journal of Molecular Structure* **2011**, *986* (1-3), 16-21.

- 40. Watson, D. E.; Martin, S. W., Short range order characterization of the na2s + sis2 glass system using raman, infrared and 29si magic angle spinning nuclear magnetic resonance spectroscopies. *Journal of Non-Crystalline Solids* **2017**, *471*, 39-50.
- 41. Kapoutsis, J. A.; Kamitsos, E. I.; Chryssikos, G. D.; Yiannopoulos, Y. D.; Patsis, A. P.; Prassas, M., Alkali sites in silicate glasses. *Chim.Chron.* **1994**, *23* (2-3), 341-346.
- 42. Borrajo, J. P.; Liste, S.; Serra, J.; González, P.; Chiussi, S.; León, B.; Pérez Amor, M.; Ylänen, H. O.; Hupa, M., Influence of the network modifier content on the bioactivity of silicate glasses. *Key Engineering Materials* **2003**, *254-256*, 23-26.
- 43. Jha, P. K.; Pandey, O. P.; Singh, K., Structural and thermal properties of na2s–p2s5 glass and glass ceramics. *Journal of Non-Crystalline Solids* **2013**, *379*, 89-94.
- 44. Ellerbrock, R.; Stein, M.; Schaller, J., Comparing amorphous silica, short-range-ordered silicates and silicic acid species by ftir. *Sci Rep* **2022**, *12* (1), 11708.
- 45. Hirai, K.; Tatsumisago, M.; Takahashi, M.; Minami, T., 29si and 31p mas-nmr spectra of li2s-sis2-li3po4 rapidly quenched glasses. *Journal of the American Ceramic Society* **2005**, *79* (2), 349-352.
- 46. Minami, K.; Mizuno, F.; Hayashi, A.; Tatsumisago, M., Structure and properties of the 70li2s · (30 -x)p2s5·xp2o5 oxysulfide glasses and glass-ceramics. *Journal of Non-Crystalline Solids* **2008**, *354* (2-9), 370-373.
- 47. Kmiec, S.; Joyce, A.; Bayko, D.; Martin, S. W., Glass formation and structure of melt quenched mixed oxy-sulfide na4p2s7-xox glasses for $0 \le x \le 5$. *Journal of Non-Crystalline Solids* **2020**, *534*.
- 48. Eckert, H.; Kennedy, J. H.; Pradel, A.; Ribes, M., Structural transformation of thiosilicate glasses: 29si mas-nmr evidence for edge-sharing in the system li2s □sis2. *Journal of Non-Crystalline Solids* **1989**, 113 (2-3), 287-293.
- 49. Torres, V., 3rd; Martin, S. W., Effects of lipon incorporation on the structures and properties of mixed oxy-sulfide-nitride glassy solid electrolytes. *Inorg Chem* **2023**, *62* (21), 8271-8284.
- 50. Charpentier, T.; Ispas, S.; Profeta, M.; Mauri, F.; Pickard, C. J., First-principles calculation of 170, 29si, and 23na nmr spectra of sodium silicate crystals and glasses. *The Journal of Physical Chemistry B* **2004**, *108* (13), 4147-4161.
- 51. Lupis, C. H. P., Chemical thermodynamics of materials. First ed.; New York, 1983; p 581.
- 52. Richards, W. D.; Miara, L. J.; Wang, Y.; Kim, J. C.; Ceder, G., Interface stability in solid-state batteries. *Chemistry of Materials* **2015**, *28* (1), 266-273.
- 53. Jain, A.; Ong, S. P.; Hautier, G.; Chen, W.; Richards, W. D.; Dacek, S.; Cholia, S.; Gunter, D.; Skinner, D.; Ceder, G.; Persson, K. A., Commentary: The materials project: A materials genome approach to accelerating materials innovation. *APL Materials* **2013**, *I* (1).
- 54. Jain, A.; Hautier, G.; Ong, S. P.; Moore, C. J.; Fischer, C. C.; Persson, K. A.; Ceder, G., Formation enthalpies by mixing gga and gga+ucalculations. *Physical Review B* **2011**, *84* (4).
- 55. Hundt, R.; Schön, J. C.; Jansen, M., Cmpz– an algorithm for the efficient comparison of periodic structures. *Journal of Applied Crystallography* **2006**, *39* (1), 6-16.
- 56. Bergerhoff, G.; Hundt, R.; Sievers, R.; Brown, I. D., The inorganic crystal structure data base. *Journal of Chemical Information and Computer Sciences* **2002**, *23* (2), 66-69.
- 57. Doweidar, H., Density–structure correlations in na2o–cao–p2o5–sio2 bioactive glasses. *Journal of Non-Crystalline Solids* **2009**, *355* (9), 577-580.
- 58. Watson, D. E.; Martin, S. W., Composition dependence of the glass-transition temperature and molar volume in sodium thiosilicophosphate glasses: A structural interpretation using a real solution model. *J Phys Chem B* **2018**, *122* (46), 10637-10646.
- 59. Sakuda, A.; Hayashi, A.; Tatsumisago, M., Sulfide solid electrolyte with favorable mechanical property for all-solid-state lithium battery. *Sci Rep* **2013**, *3*, 2261.
- 60. Rajendran, V.; Begum, A. N.; Azooz, M. A.; el Batal, F. H., Microstructural dependence on relevant physical-mechanical properties on sio2-na2o-cao-p2o5 biological glasses. *Biomaterials* **2002**, *23* (21), 4263-75.
- 61. Martin, S. W.; Angell, C. A., D.C. And a.C. Conductivity in wide composition range lithium oxide-phosphorus oxide (li20-p205) glasses. *Journal of Non-Crystalline Solids* **1986**, *83* (1-2), 185-207.

- 62. Kmiec, S. J.; Lovi, J. M.; Joyce, A.; Bayko, D.; Martin, S. W., Anomalously strong viscosity behavior in mixed oxy-sulfide na4p2s7-xox invert glasses. *Journal of Non-Crystalline Solids* **2021**, *553*.
- 63. Wilkinson, C. J.; Doss, K.; Cassar, D. R.; Welch, R. S.; Bragatto, C. B.; Mauro, J. C., Predicting ionic diffusion in glass from its relaxation behavior. *J Phys Chem B* **2020**, *124* (6), 1099-1103.
- 64. Christensen, R.; Olson, G.; Martin, S. W., Ionic conductivity of mixed glass former 0.35na(2)o + 0.65[xb(2)o(3) + (1 x)p(2)o(5)] glasses. *J Phys Chem B* **2013**, *117* (51), 16577-86.
- 65. Anderson, O. L.; Stuart, D. A., Calculation of activation energy of ionic conductivity in silica glasses by classical methods. *Journal of the American Ceramic Society* **2006**, *37* (12), 573-580.
- 66. Martin, S. W.; Bischoff, C.; Schuller, K., Composition dependence of the na(+) ion conductivity in 0.5na2s + 0.5[xges2 + (1 x)ps5/2] mixed glass former glasses: A structural interpretation of a negative mixed glass former effect. *J Phys Chem B* **2015**, *119* (51), 15738-51.
- 67. Glasser, L., Solid-state energetics and electrostatics: Madelung constants and madelung energies. *Inorg Chem* **2012**, *51* (4), 2420-4.
- 68. Mestechkin, M. M., Electrostatic parameters of ionic crystals. *Journal of Physical and Chemical Reference Data* **2000**, *29* (4), 571-595.
- 69. Swenson, J.; Matic, A.; Karlsson, C.; Börjesson, L.; Meneghini, C.; Howells, W. S., Random ion distribution model: A structural approach to the mixed-alkali effect in glasses. *Physical Review B* **2001**, 63 (13).